Arbitrary high order accurate space–time discontinuous Galerkin finite element schemes on staggered unstructured meshes for linear elasticity

Maurizio Tavelli, Michael Dumbser

Department of Civil, Environmental and Mechanical Engineering, University of Trento, Via Mesiano 77, I-38123 Trento, Italy

A B S T R A C T

In this paper we propose a new high order accurate space–time discontinuous Galerkin (DG) finite element scheme for the solution of the linear elastic wave equations in first order velocity-stress formulation in two and three-space dimensions on *staggered* unstructured triangular and tetrahedral meshes. The method reaches arbitrary high order of accuracy in both space and time via the use of space–time basis and test functions. Within the staggered mesh formulation, we define the discrete velocity field in the control volumes of a primary mesh, while the discrete stress tensor is defined on a face-based staggered dual mesh. The space–time DG formulation leads to an *implicit* scheme that requires the solution of a linear system for the unknown degrees of freedom at the new time level. The number of unknowns is reduced at the aid of the Schur complement, so that in the end only a linear system for the degrees of freedom of the velocity field needs to be solved, rather than a system that involves both stress and velocity. Thanks to the use of a spatially staggered mesh, the stencil of the final velocity system involves only the element and its direct neighbors and the linear system can be efficiently solved via matrix-free iterative methods. Despite the necessity to solve a linear system, the numerical scheme is still computationally efficient. The chosen discretization and the linear nature of the governing PDE system lead to an unconditionally stable scheme, which allows large time steps even for low quality meshes that contain so-called sliver elements. The fully discrete staggered space–time DG method is proven to be *energy stable* for any order of accuracy, for any mesh and for any time step size. For the particular case of a simple Crank–Nicolson time discretization and homogeneous material, the final velocity system can be proven to be symmetric and positive definite and in this case the scheme is also exactly *energy preserving*. The new scheme is applied to several test problems in two and three space dimensions, providing also a comparison with high order explicit ADER-DG schemes.

© 2018 The Author(s). Published by Elsevier Inc. This is an open access article under the CC BY-NC-ND license (http://creativecommons.org/licenses/by-nc-nd/4.0/).

1. Introduction

Even nowadays the accurate simulation of elastic wave propagation in heterogeneous media involving complex geometries is a very challenging task. In the past several numerical methods have been developed in order to solve the linear elasticity equations. Some classical finite difference methods can be found in [1–3] and for further extensions and develop-

ments see, e.g. [4–10]. Concerning the class of pseudo-spectral methods we refer the reader to [11,12]. The spectral finite element method, originally introduced by Patera in [13], was applied to linear elastic wave propagation in a well-known series of papers, see e.g. [14–18] and references therein. We also mention here alternative developments in the field of stabilized continuous finite elements for elastic and acoustic wave propagation based on the velocity stress formulation, see e.g. [19–21].

A major challenge in the numerical simulation of linear elastic waves is the ability of the numerical scheme to accurately propagate complex wave patterns over long distances and for very long times. Therefore, the use of high order schemes in both space and time is necessary. For a quantitative accuracy analysis of high order schemes applied to elastic wave propagation, see e.g. [22,23]. The analysis is based on the misfit criteria developed in [24,25]. For an alternative study of high order DG schemes applied to wave propagation problems we refer to [26].

Another challenge is the discretization of complex geometries including both, complex surface topography as well as complex sub-surface fault structures. In this case, the use of unstructured simplex meshes composed of triangles or tetra-hedra seems to be beneficial concerning the problem of mesh generation in complex geometries. Concerning high order explicit discontinuous Galerkin (DG) finite element schemes for linear elastic wave propagation on general unstructured meshes the reader is referred to [27–31] and to [32–34]. However, since the previous methods are *explicit*, they are only stable under a CFL-type stability condition on the time step that depends on the mesh quality as well as the polynomial approximation degree used. In particular, unstructured simplex meshes for complex 3D geometries may contain so-called sliver elements, which are tiny elements with very bad aspect ratio and which look like needles or thin plates. In the case of explicit time discretizations, such elements can be efficiently treated only at the aid of time-accurate local time stepping (LTS), see e.g. [31,35–39]. In this paper, we try to solve this problem in a different way using an efficient high order accurate *implicit* time discretization.

Our work is inspired by a new class of high order accurate semi-implicit discontinuous Galerkin finite element schemes on staggered meshes recently introduced in [40–46] for the numerical solution of the shallow water equations, the incompressible and the compressible Navier–Stokes equations. Being semi-implicit, the previous methods allow large time steps. Furthermore, the use of an edge-based staggered grid allows to connect the discrete divergence operator with the discrete gradient operator. This leads to some interesting properties of the final pressure system that needs to be solved, which becomes symmetric and positive definite. The use of staggered meshes is state of the art for many finite difference schemes used in computational fluid dynamics [47–57] as well as for seismic wave propagation [6,58–60]. However, at present staggered meshes are still almost unknown in the context of high order discontinuous Galerkin finite element methods for wave propagation. Apart from the above-mentioned references on semi-implicit staggered DG schemes [40–46], the authors are only aware of [61–65] and references therein concerning high order DG schemes for wave propagation using edge-based staggered grids. For central DG schemes, which use a vertex-based grid staggering, the reader is referred to [66,67]. However, none of those references uses space–time discontinuous Galerkin finite elements, where the basis and test functions depend not only on space, but both on space and time. The concept of space–time DG schemes was introduced by van der Vegt et al. for computational fluid dynamics in [68–72] and has been subsequently analyzed e.g. in [73,74]. The first application of space–time DG schemes to elastodynamics on collocated grids has been reported in [75,76], but to the best of our knowledge there exists no space–time DG scheme for the linear elastic wave equations on staggered grids so far. It is the aim of this paper to design and analyze the properties of such methods.

More precisely, in this paper we extend the idea of staggered semi-implicit space–time discontinuous Galerkin methods for the Navier–Stokes equations [42,43,45,44] to linear elasticity. While the velocity field is discretized on the main grid, the stress tensor is defined on a face-based staggered *dual* mesh. The governing PDE system is linear and all terms are taken implicitly. Inserting the discrete evolution equations for the stress tensor into the discrete momentum equation leads to one single linear system for the velocity field via the application of the Schur complement. Once the velocity field at the new time is known, one can readily update the stress tensor using an explicit formula. The good properties of the main system already observed in [43,45] are achieved also in this case. The resulting numerical scheme is shown to be *energy stable* for any polynomial degree in space and time. A remarkable particular case can be obtained by using arbitrary high order polynomials in space combined with a second order Crank–Nicolson time discretization. For this special case the method becomes exactly energy preserving and the main system becomes symmetric and positive definite. We also present a simple and efficient physics-based preconditioner that is useful in the presence of sliver elements.

The rest of this paper is organized as follows: in Section 2 we present the governing PDE system and in Section 3 we introduce the staggered grid that is used in our approach, as well as the chosen basis functions. In Section 4 we present the numerical scheme and analyze its properties in Section 5. In Section 6 we show numerical results for several test problems in two and three space dimensions. We compare all numerical results obtained with our new high order staggered space–time DG scheme with those obtained by a high order explicit ADER-DG scheme on unstructured meshes. The paper closes with some concluding remarks and an outlook to future work in Section 7.

2. Governing equations

Based on the theory of linear elasticity, see e.g. [77], the governing partial differential equations for the wave propagation in a linear elastic medium without attenuation can be written in compact first order velocity-stress formulation based on the Hooke law and the momentum conservation law. They read

$$\frac{\partial \boldsymbol{\sigma}}{\partial t} - \mathbf{E} \cdot \nabla \mathbf{v} = \boldsymbol{S}_{\sigma}, \tag{1}$$

$$\frac{\partial \rho \mathbf{v}}{\partial t} - \nabla \cdot \boldsymbol{\sigma} = \rho \boldsymbol{S}_{v}, \tag{2}$$

where ρ is the mass density, $\boldsymbol{\sigma} = \boldsymbol{\sigma}^{\top}$ is the symmetric stress tensor, $\mathbf{v} = (u, v, w)$ is the velocity field, $\boldsymbol{S}_{v}$ and $\boldsymbol{S}_{\sigma}$ are volume sources and $\mathbf{E}$ denotes the usual rank 4 stiffness tensor representing the linear material behavior according to the Hooke law $\sigma_{ij} = E_{ijkl}\epsilon_{kl}$, where $\epsilon_{kl} = \epsilon_{lk}$ is the symmetric strain tensor. The connection between the strain *rate* tensor and the velocity gradient is $\partial_t \epsilon_{ij} = \dot{\epsilon}_{ij} = \frac{1}{2}(\partial_j v_i + \partial_i v_j)$. It is well-known that the stiffness tensor $\mathbf{E}$ has the following so-called *minor symmetries* $E_{ijkl} = E_{jikl} = E_{ijlk}$, due to the symmetries of the stress and the strain tensor, and the *major symmetry* $E_{ijkl} = E_{klij}$, hence it can have at most 21 independent components, and not 81. From the minor symmetries of $\mathbf{E}$ follows that $E_{ijkl}\partial_t \epsilon_{kl} = \frac{1}{2}E_{ijkl}\partial_l v_k + \frac{1}{2}E_{ijlk}\partial_k v_l = E_{ijkl}\partial_l v_k = \mathbf{E} \cdot \nabla \mathbf{v}$. Throughout the paper we use the Einstein summation convention over repeated indices. The symmetric stress tensor $\boldsymbol{\sigma}$ is

$$\boldsymbol{\sigma} = \begin{pmatrix} \sigma_{xx} & \sigma_{xy} & \sigma_{xz} \\ \sigma_{xy} & \sigma_{yy} & \sigma_{yz} \\ \sigma_{xz} & \sigma_{yz} & \sigma_{zz} \end{pmatrix} = \boldsymbol{\sigma}^{T}. \tag{3}$$

The normal stress components along the x, y and z directions are given by σ_{xx}, σ_{yy} and σ_{zz}, while the shear stresses are represented by σ_{xy}, σ_{xz} and σ_{yz}. Due to its symmetry the stress tensor $\boldsymbol{\sigma}$ can be written as a vector in terms of its six independent components as $\tilde{\boldsymbol{\sigma}} = (\sigma_{xx}, \sigma_{yy}, \sigma_{zz}, \sigma_{yz}, \sigma_{xz}, \sigma_{xy})$, where we use the tilde symbol when we refer to the vector of the six independent components of the stress tensor $\boldsymbol{\sigma}$. The same notation is also used for the 6 independent components of the strain tensor, i.e. $\tilde{\boldsymbol{\epsilon}} = (\epsilon_{xx}, \epsilon_{yy}, \epsilon_{zz}, \epsilon_{yz}, \epsilon_{xz}, \epsilon_{xy})$, so that the stress-strain relationship can be also written as $\tilde{\boldsymbol{\sigma}} = \tilde{\mathbf{E}}\tilde{\boldsymbol{\epsilon}}$. In this paper we assume $\tilde{\mathbf{E}}$ to be *invertible* so that the strain can be computed from the stress as $\tilde{\boldsymbol{\epsilon}} = \tilde{\mathbf{E}}^{-1}\tilde{\boldsymbol{\sigma}}$. From $\tilde{\mathbf{E}}^{-1}$ we define a tensorial object $\mathbf{E}^{-1} = E_{ijkl}^{-1}$ with the same symmetries as E_{ijkl} and the property $E_{ijpq}^{-1}E_{pqkl} = \delta_{ijkl}$. The object δ_{ijkl} has again the same symmetries as $\mathbf{E}$ and furthermore it satisfies $\delta_{ijkl}\sigma_{kl} = \sigma_{ij}$ and thus also $\delta_{ijkl}\sigma_{ij} = \sigma_{kl}$. The entries of E_{ijkl}^{-1} are given by those of $\tilde{\mathbf{E}}^{-1}$ or are scaled by one half, and the object δ_{ijkl} contains only zeros, ones and $\frac{1}{2}$. Their construction is immediate once the inverse $\tilde{\mathbf{E}}^{-1}$ has been computed. For *isotropic material*, equation (1) can be rewritten in terms of the two Lamé constants λ and μ simply as

$$\partial_t \boldsymbol{\sigma} - \lambda (\nabla \cdot \mathbf{v}) \mathbf{I} - \mu \left(\nabla \mathbf{v} + \nabla \mathbf{v}^T \right) = \boldsymbol{S}_{\sigma}, \tag{4}$$

with the identity matrix $\mathbf{I}$, or in terms of the vector $\tilde{\boldsymbol{\sigma}}$ and the independent components of the strain rate tensor as

$$\partial_t \tilde{\boldsymbol{\sigma}} - \tilde{\mathbf{E}} \cdot \partial_t \tilde{\boldsymbol{\epsilon}} = \boldsymbol{S}_{\tilde{\sigma}}, \tag{5}$$

with $\partial_t \tilde{\boldsymbol{\epsilon}} = \left(\partial_x u, \partial_y v, \partial_z w, \frac{1}{2}(\partial_z v + \partial_y w), \frac{1}{2}(\partial_z u + \partial_x w), \frac{1}{2}(\partial_y u + \partial_x v) \right)$ and where for isotropic material

$$\tilde{\mathbf{E}} = \begin{pmatrix} \lambda + 2\mu & \lambda & \lambda & 0 & 0 & 0 \\ \lambda & \lambda + 2\mu & \lambda & 0 & 0 & 0 \\ \lambda & \lambda & \lambda + 2\mu & 0 & 0 & 0 \\ 0 & 0 & 0 & 2\mu & 0 & 0 \\ 0 & 0 & 0 & 0 & 2\mu & 0 \\ 0 & 0 & 0 & 0 & 0 & 2\mu \end{pmatrix}, \quad \tilde{\mathbf{E}}^{-1} = \frac{1}{2\mu\alpha} \begin{pmatrix} 2(\lambda + \mu) & -\lambda & -\lambda & 0 & 0 & 0 \\ -\lambda & 2(\lambda + \mu) & -\lambda & 0 & 0 & 0 \\ -\lambda & -\lambda & 2(\lambda + \mu) & 0 & 0 & 0 \\ 0 & 0 & 0 & \alpha & 0 & 0 \\ 0 & 0 & 0 & 0 & \alpha & 0 \\ 0 & 0 & 0 & 0 & 0 & \alpha \end{pmatrix},$$

$$\tag{6}$$

with $\alpha = 3\lambda + 2\mu$. For a homogeneous material we can assume $\mathbf{E}$ to be a constant in space and time. For non-homogeneous media we have $\mathbf{E} = \mathbf{E}(\mathbf{x})$, which, however, is still assumed to be a constant in time.

3. Staggered unstructured grid and basis functions

Throughout this paper we use the same unstructured spatially staggered mesh as the one used in [78,42,43] for the two and three-dimensional case, respectively. In the following section we briefly summarize the grid construction and the main notation for the two dimensional triangular grid. After that, the primary and dual spatial elements are extended to the three dimensional case and also to the case of space–time control volumes.

Two space dimensions. In the two-dimensional case the spatial computational domain $\Omega \subset \mathbb{R}^2$ is covered with a set of N_i non-overlapping triangular elements $\boldsymbol{T}_i$ with $i = 1 \ldots N_i$. By denoting with N_j the total number of edges, the j-th edge will be called Γ_j. $\mathcal{B}(\Omega)$ denotes the set of indices j corresponding to boundary edges. The three edges of each triangle $\boldsymbol{T}_i$ constitute the set S_i defined by $S_i = \{ j \in [1, N_j] \mid \Gamma_j \text{ is an edge of } \boldsymbol{T}_i \}$. For every $j \in [1 \ldots N_j] - \mathcal{B}(\Omega)$ there exist two triangles i_1 and i_2 that share Γ_j. We assign arbitrarily a left and a right triangle called respectively $\ell(j)$ and $r(j)$ for any
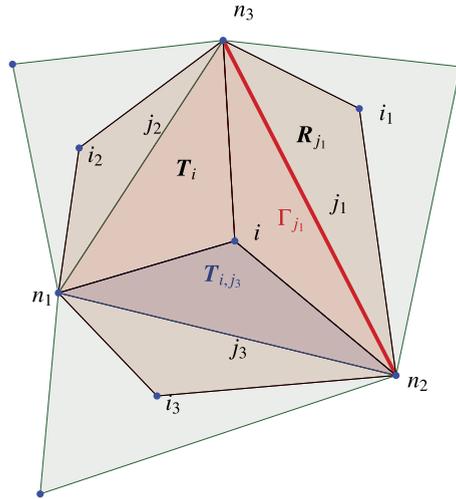
Fig. 1. Example of a triangular mesh element with its three neighbors and the associated staggered edge-based dual control volumes, together with the notation used throughout the paper.
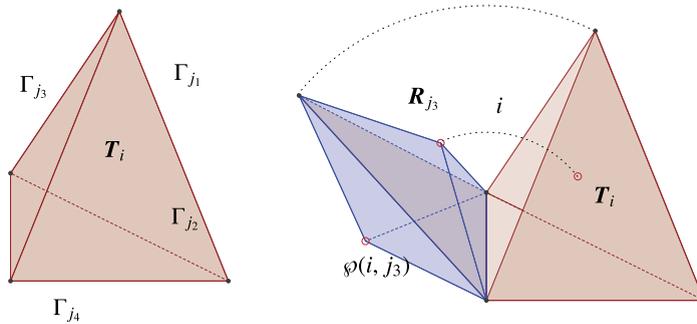

Fig. 2. An example of a tetrahedral element of the primary mesh with $S_i = \{j_1, j_2, j_3, j_4\}$ (left) a non-standard dual face-based hexahedral element associated to the face j_3 (right).

$j \in [1 \ldots N_j] - \mathcal{B}(\Omega)$. The standard positive direction is assumed to be from left to right. $\mathbf{n}_j$ denotes the unit normal vector defined on the edge j and oriented with respect to the positive direction according to the previous definition. For every triangular element i and edge $j \in S_i$, the index of the neighbor triangle of element $\boldsymbol{T}_i$ that shares the edge Γ_j is denoted by $\wp(i, j)$.

For every $j \in [1, N_j] - \mathcal{B}(\Omega)$ the quadrilateral dual element associated to Γ_j is called $\boldsymbol{R}_j$ and it is defined, in general, by the two barycenter of $\boldsymbol{T}_{\ell(j)}$ and $\boldsymbol{T}_{r(j)}$ and the two nodes of Γ_j, see also [79–82,41,61]. We denote by $\boldsymbol{T}_{i,j} = \boldsymbol{R}_j \cap \boldsymbol{T}_i$ the intersection element for every i and $j \in S_i$. Fig. 1 summarizes the used notation, the primal triangular mesh and the dual quadrilateral grid. According to [42], we will call the mesh of triangular elements $\{\boldsymbol{T}_i\}_{i\in[1,N_i]}$ the *main grid* and the quadrilateral grid $\{\boldsymbol{R}_j\}_{j\in[1,N_d]}$ is termed the *dual grid*.

Three space dimensions. The definitions given above are then readily extended to three space dimensions with the domain $\Omega \subset \mathbb{R}^3$. An example of the resulting main and dual grid in three space dimensions is reported in Fig. 2. The main grid consists of tetrahedral simplex elements, and the face-based dual elements contain the three vertices of the common triangular face of two tetrahedra (a left and a right one), and the two barycenters of the two tetrahedra that share the same face. In three space dimensions the dual grid therefore consists of non-standard five-point hexahedral elements. The same face-based staggered dual mesh has also been used in [80,80–83].

Space–time extension. In the time direction we cover the time interval $[0, T]$ with a sequence of times $0 = t^0 < t^1 < t^2 \ldots < t^N < t^{N+1} = T$. We denote the time step by $\Delta t^{n+1} = t^{n+1} - t^n$ and the corresponding time interval by $T^{n+1} = [t^n, t^{n+1}]$ for $n = 0 \ldots N$. In order to ease notation, sometimes we will use the abbreviation $\Delta t = \Delta t^{n+1}$. The generic space–time element defined in the time interval $[t^n, t^{n+1}]$ is given by $\boldsymbol{T}_i^{st} = \boldsymbol{T}_i \times T^{n+1}$ for the main grid, and $\boldsymbol{R}_j^{st} = \boldsymbol{R}_j \times T^{n+1}$ for the dual grid.

Space–time basis functions. According to [41–43] we proceed as follows: in the two dimensional case, we first construct the polynomial basis up to a generic polynomial degree p on some triangular and quadrilateral reference elements. In particular, we take $T_{std} = \{(\xi, \eta) \in \mathbb{R}^2 \mid 0 \le \xi \le 1, \, 0 \le \eta \le 1 - \xi\}$ as the reference triangle. Using the standard nodal approach of

conforming continuous finite elements, we obtain $N_\phi = \frac{(p+1)(p+2)}{2}$ basis functions $\{\phi_k\}_{k\in[1,N_\phi]}$ on T_{std} and $N_\psi = (p+1)^2$ nodal basis functions on the unit square $R_{std} = [0,1]^2$ that can be obtained using the tensor product of one dimensional basis functions defined of the unit interval $[0,1]$. The connection between the reference coordinates $\boldsymbol{\xi} = (\xi, \eta)$ and the physical coordinates $\mathbf{x} = (x, y)$ is obtained using either sub-parametric or iso-parametric maps, see e.g. [41] for more details.

Regarding the basis functions in three space dimensions, we use the unit tetrahedron $T_{std} = \{(\xi, \eta, \zeta) \in \mathbb{R}^3 \mid 0 \leq \xi \leq 1, 0 \leq \eta \leq 1 - \xi, 0 \leq \zeta \leq 1 - \xi - \eta\}$ to construct the basis polynomials for the main grid. We use again the standard nodal basis functions of conforming finite elements based on the reference element T_{std} and then using either a sub-parametric or an iso-parametric map to connect the reference space $\boldsymbol{\xi} = (\xi, \eta, \zeta)$ to the physical space $\mathbf{x} = (x, y, z)$ and vice-versa. For the non-standard five-point hexahedral elements of the dual mesh, we define the polynomial basis directly in the physical space via the rescaled monomials of a Taylor series, as defined in [43]. We thus obtain $N_\phi = N_\psi = \frac{(p+1)(p+2)(p+3)}{6}$ basis functions per element for both, the main grid and the dual mesh.

Finally, we construct the time basis functions on a reference interval $I_{std} = [0,1]$ for polynomials of degree p_γ by taken the Lagrange interpolation polynomials passing through the Gauss–Legendre quadrature points for the unit interval I_{std}. In this case the resulting $N_\gamma = p_\gamma + 1$ basis functions in time are called $\{\gamma_k\}_{k\in[1,N_\gamma]}$. In this manner, the nodal basis in time is an orthogonal basis. For every time interval $[t^n, t^{n+1}]$, the map between the reference interval and the physical one is simply given by $t = t^n + \tau \Delta t^{n+1}$ $\forall \tau \in [0,1]$. Using the tensor product we can finally construct the basis functions on the space–time elements T_i^{st} and R_j^{st} as $\tilde{\phi}(\boldsymbol{\xi}, \tau) = \phi(\boldsymbol{\xi}) \cdot \gamma(\tau)$ and $\tilde{\psi}(\boldsymbol{\xi}, \tau) = \psi(\boldsymbol{\xi}) \cdot \gamma(\tau)$. The total number of basis functions becomes $N_\phi^{st} = N_\phi \cdot N_\gamma$ and $N_\psi^{st} = N_\psi \cdot N_\gamma$.

4. Numerical scheme

The discrete velocity field $\mathbf{v}_h$ is now defined on the main grid, while the discrete stress tensor $\boldsymbol{\sigma}_h$ is defined on the face-based staggered dual grid, namely $\mathbf{v}_i(\mathbf{x}, t) = \mathbf{v}_h(\mathbf{x}, t)|_{T_i^{st}}$ and $\boldsymbol{\sigma}_j(\mathbf{x}, t) = \boldsymbol{\sigma}_h(\mathbf{x}, t)|_{R_j^{st}}$. For a heterogeneous material also the material parameters λ, μ and ρ have to be discretized using piecewise high order polynomials. The discrete material density ρ_h is defined on the main grid, while the discrete material tensor $\mathbf{E}_h$ is defined on the dual grid, namely $\rho_i(\mathbf{x}) = \rho_h(\mathbf{x})|_{T_i^{st}}$ and $\mathbf{E}_j(\mathbf{x}) = \mathbf{E}_h(\mathbf{x})|_{R_j^{st}}$. The numerical solution of (1)–(2), as well as the discrete material parameters are represented inside the space–time control volumes of the main and the dual grid and for a time slice T^{n+1} by piecewise space–time polynomials as follows:

$$\mathbf{v}_i(\mathbf{x}, t) = \sum_{l=1}^{N_\phi^{st}} \tilde{\phi}_l^{(i)}(\mathbf{x}, t) \hat{\mathbf{v}}_{l,i}^{n+1} =: \tilde{\boldsymbol{\phi}}^{(i)}(\mathbf{x}, t) \hat{\mathbf{v}}_i^{n+1},$$

$$\rho_i(\mathbf{x}, t) = \sum_{l=1}^{N_\phi^{st}} \tilde{\phi}_l^{(i)}(\mathbf{x}, t) \hat{\mathbf{v}}_{l,i}^{n+1} =: \tilde{\boldsymbol{\phi}}^{(i)}(\mathbf{x}, t) \hat{\rho}_i^{n+1},$$

$$\boldsymbol{\sigma}_j(\mathbf{x}, t) = \sum_{l=1}^{N_\psi^{st}} \tilde{\psi}_l^{(j)}(\mathbf{x}, t) \hat{\sigma}_{l,j}^{n+1} =: \tilde{\boldsymbol{\psi}}^{(j)}(\mathbf{x}, t) \hat{\boldsymbol{\sigma}}_j^{n+1},$$

$$\mathbf{E}_j(\mathbf{x}) = \sum_{l=1}^{N_\psi^{st}} \tilde{\psi}_l^{(j)}(\mathbf{x}) \hat{\mathbf{E}}_{l,j} =: \tilde{\boldsymbol{\psi}}^{(j)}(\mathbf{x}) \hat{\mathbf{E}}_j. \tag{7}$$

Note that the discrete velocity is allowed to jump at the element boundaries of the main grid, while the discrete stress tensor jumps only at the boundaries of the dual grid and is therefore *continuous* across the boundaries of the main grid. This property is essential for our staggered DG method, since it completely avoids the necessity of Riemann solvers or numerical flux functions at the element boundaries.

Multiplication of the momentum equation (2) by a test function $\tilde{\phi}_k$, for $k = 1 \ldots N_\phi^{st}$, and integration over a primary space–time control volume T_{st}, leads to

$$\int_{T_i^{st}} \tilde{\phi}_k^{(i)} \frac{\partial \rho \mathbf{v}}{\partial t} d\mathbf{x} \, dt - \int_{T_i^{st}} \tilde{\phi}_k^{(i)} \nabla \cdot \boldsymbol{\sigma} \, d\mathbf{x} \, dt = \int_{T_i^{st}} \tilde{\phi}_k^{(i)} \rho \boldsymbol{S}_v d\mathbf{x} \, dt. \tag{8}$$

Using integration by parts Eqn. (8) yields

$$\int_{T_i^{st}} \tilde{\phi}_k^{(i)} \frac{\partial \rho \mathbf{v}}{\partial t} d\mathbf{x} \, dt - \left(\int_{\partial T_i^{st}} \tilde{\phi}_k^{(i)} \boldsymbol{\sigma} \cdot \mathbf{n}_i dS \, dt - \int_{T_i^{st}} \nabla \tilde{\phi}_k^{(i)} \cdot \boldsymbol{\sigma} d\mathbf{x} \, dt \right) = \int_{T_i^{st}} \tilde{\phi}_k^{(i)} \rho \boldsymbol{S}_v d\mathbf{x} \, dt, \tag{9}$$

where $\mathbf{n}_i$ indicates the outward unit normal vector with respect to $\boldsymbol{T}_i$. Multiplication of equation (1) by a test function $\tilde{\psi}_k$, for $k = 1 \ldots N_\psi^{st}$ and integration over a dual space–time control volume $\boldsymbol{R}_j^{st}$ leads to

$$\int\limits_{\boldsymbol{R}_j^{st}} \tilde{\psi}_k^{(j)} \frac{\partial \boldsymbol{\sigma}}{\partial t} d\mathbf{x} \, dt \; - \int\limits_{\boldsymbol{R}_j^{st}} \tilde{\psi}_k^{(j)} \mathbf{E} \cdot \nabla \mathbf{v} d\mathbf{x} \, dt \; = \int\limits_{\boldsymbol{R}_j^{st}} \tilde{\psi}_k^{(j)} \boldsymbol{S}_\sigma \, d\mathbf{x} \, dt \, . \tag{10}$$

Due to the discontinuous discretization of our numerical quantities we have to split equations (9) and (10) as follows:

$$\int\limits_{\boldsymbol{T}_i^{st}} \phi_k^{(i)} \frac{\partial (\rho \mathbf{v})_i}{\partial t} d\mathbf{x} \, dt \; - \sum_{j \in S_i} \left(\int\limits_{\Gamma_j^{st}} \tilde{\phi}_k^{(i)} \boldsymbol{\sigma}_j \cdot \mathbf{n}_{i,j} dS \, dt \; - \int\limits_{\boldsymbol{T}_{i,j}^{st}} \nabla \tilde{\phi}_k^{(i)} \cdot \boldsymbol{\sigma}_j d\mathbf{x} \, dt \right) = \int\limits_{\boldsymbol{T}_i^{st}} \tilde{\phi}_k^{(i)} \rho \boldsymbol{S}_v \, d\mathbf{x} \, dt \, , \tag{11}$$

$$\int\limits_{\boldsymbol{R}_j^{st}} \tilde{\psi}_k^{(j)} \frac{\partial \boldsymbol{\sigma}_j}{\partial t} d\mathbf{x} \, dt \; - \int\limits_{\boldsymbol{T}_{\ell(j),j}^{st}} \tilde{\psi}_k^{(j)} \mathbf{E}_j \cdot \nabla \mathbf{v}_{\ell(j)} d\mathbf{x} \, dt \; - \int\limits_{\boldsymbol{T}_{r(j),j}^{st}} \tilde{\psi}_k^{(j)} \mathbf{E}_j \cdot \nabla \mathbf{v}_{r(j)} d\mathbf{x} \, dt \; - \int\limits_{\Gamma_j^{st}} \tilde{\psi}_k^{(j)} \mathbf{E}_j \cdot (\mathbf{v}_{r(j)} - \mathbf{v}_{\ell(j)}) \otimes \mathbf{n}_j dS \, dt$$

$$= \int\limits_{\boldsymbol{R}_j^{st}} \tilde{\psi}_k^{(j)} \boldsymbol{S}_\sigma \, d\mathbf{x} \, dt \, . \tag{12}$$

With $\mathbf{n}_{i,j}$ we denote the outward pointing unit normal vector of element $\boldsymbol{T}_i^{st}$ on its face Γ_j^{st}. Note that a jump contribution is necessary in Eq. (12), since the gradient of the velocity needs to be integrated in the sense of distributions. However, since the stress tensor $\boldsymbol{\sigma}_j$ is defined on the staggered dual mesh and therefore is continuous across primary element interfaces, no Riemann solver (numerical flux function) is needed in our approach, which is a particular feature of the chosen staggered mesh. Following the ideas used in [43,42] we integrate the terms including the time derivatives in (11)–(12) by parts in time and hence obtain

$$\int\limits_{\boldsymbol{T}_i^{st}} \tilde{\phi}_k^{(i)} \frac{\partial (\rho \mathbf{v})_i}{\partial t} d\mathbf{x} \, dt = \int\limits_{\boldsymbol{T}_i} \tilde{\phi}_k^{(i)}(\mathbf{x}, t^{n+1,-}) \rho \mathbf{v}_i(\mathbf{x}, t^{n+1,-}) d\mathbf{x} \; - \int\limits_{\boldsymbol{T}_i} \tilde{\phi}_k^{(i)}(\mathbf{x}, t^{n,+}) \rho \mathbf{v}_i(\mathbf{x}, t^{n,-}) d\mathbf{x} \; - \int\limits_{\boldsymbol{T}_i^{st}} \frac{\partial \tilde{\phi}_k^{(i)}}{\partial t} (\rho \mathbf{v})_i d\mathbf{x} \, dt \, ,$$

$$\int\limits_{\boldsymbol{R}_j^{st}} \tilde{\psi}_k^{(j)} \frac{\partial \boldsymbol{\sigma}_j}{\partial t} d\mathbf{x} \, dt = \int\limits_{\boldsymbol{R}_j} \tilde{\psi}_k^{(j)}(\mathbf{x}, t^{n+1,-}) \boldsymbol{\sigma}_j(\mathbf{x}, t^{n+1,-}) d\mathbf{x} \; - \int\limits_{\boldsymbol{R}_j} \tilde{\psi}_k^{(j)}(\mathbf{x}, t^{n,+}) \boldsymbol{\sigma}_j(\mathbf{x}, t^{n,-}) d\mathbf{x} \; - \int\limits_{\boldsymbol{R}_j^{st}} \frac{\partial \tilde{\psi}_k^{(j)}}{\partial t} \sigma_j d\mathbf{x} \, dt \, , \tag{13}$$

where $t^{n,-}$ indicates the boundary-extrapolated value from a lower time slice and thus corresponds to upwinding in time, due to the causality principle. Using the definitions (7) and rewriting the contribution of the time derivative as specified in (13) we obtain from the previous equations

$$\left(\int\limits_{\boldsymbol{T}_i} \tilde{\phi}_k^{(i)}(\mathbf{x}, t^{n+1,-}) \tilde{\phi}_m^{(i)}(\mathbf{x}, t^{n+1,-}) d\mathbf{x} \; - \int\limits_{\boldsymbol{T}_i^{st}} \frac{\partial \tilde{\phi}_k^{(i)}}{\partial t} \tilde{\phi}_m^{(i)} d\mathbf{x} \, dt \right) (\hat{\rho} \mathbf{v})_{m,i}^{n+1} \; - \int\limits_{\boldsymbol{T}_i} \tilde{\phi}_k^{(i)}(\mathbf{x}, t^{n,+}) \tilde{\phi}_m^{(i)}(\mathbf{x}, t^{n,-}) d\mathbf{x} \, (\hat{\rho} \mathbf{v})_{m,i}^{n}$$

$$- \sum_{j \in S_i} \left(\int\limits_{\Gamma_j^{st}} \tilde{\phi}_k^{(i)} \tilde{\psi}_m^{(j)} \mathbf{n}_{i,j} dS \, dt \; - \int\limits_{\boldsymbol{T}_{i,j}^{st}} \nabla \tilde{\phi}_k^{(i)} \tilde{\psi}_m^{(j)} d\mathbf{x} \, dt \right) \cdot \hat{\boldsymbol{\sigma}}_{m,j}^{n+1} = \int\limits_{\boldsymbol{T}_i^{st}} \tilde{\phi}_k^{(i)} \rho \boldsymbol{S}_v \, d\mathbf{x} \, dt \tag{14}$$

and

$$\left(\int\limits_{\boldsymbol{R}_j} \tilde{\psi}_k^{(i)}(\mathbf{x}, t^{n+1,-}) \tilde{\psi}_m^{(i)}(\mathbf{x}, t^{n+1,-}) d\mathbf{x} \; - \int\limits_{\boldsymbol{R}_j^{st}} \frac{\partial \tilde{\psi}_k^{(i)}}{\partial t} \tilde{\psi}_m^{(i)} d\mathbf{x} \, dt \right) \hat{\boldsymbol{\sigma}}_{m,j}^{n+1} \; - \int\limits_{\boldsymbol{R}_i} \tilde{\psi}_k^{(i)}(\mathbf{x}, t^{n,+}) \tilde{\psi}_m^{(i)}(\mathbf{x}, t^{n,-}) d\mathbf{x} \, \hat{\boldsymbol{\sigma}}_{m,j}^{n}$$

$$- \hat{\mathbf{E}}_{q,j} \cdot \left(\int\limits_{\boldsymbol{T}_{\ell(j),j}^{st}} \tilde{\psi}_k^{(j)} \nabla \tilde{\phi}_m^{(\ell(j))} \tilde{\psi}_q^{(j)} d\mathbf{x} \, dt \; - \int\limits_{\Gamma_j^{st}} \tilde{\psi}_k^{(j)} \tilde{\phi}_m^{(\ell(j))} \tilde{\psi}_q^{(j)} \mathbf{n}_j dS dt \right) \hat{\mathbf{v}}_{m,\ell(j)}^{n+1}$$

$$-\hat{\mathbf{E}}_{q,j} \cdot \left(\int\limits_{\mathbf{T}^{st}_{r(j),j}} \tilde{\psi}^{(j)}_k \nabla \tilde{\phi}^{(r(j))}_m \tilde{\psi}^{(j)}_q d\mathbf{x}dt + \int\limits_{\Gamma^{st}_j} \tilde{\psi}^{(j)}_k \tilde{\phi}^{(r(j))}_m \tilde{\psi}^{(j)}_q \mathbf{n}_j dSdt \right) \hat{\mathbf{v}}^{n+1}_{m,r(j)} = \int\limits_{\mathbf{R}^{st}_j} \tilde{\psi}^{(j)}_k \mathbf{S}_\sigma d\mathbf{x}dt , \tag{15}$$

where the quantity $(\hat{\rho}\mathbf{v})^{n+1}_{m,i}$ is simply defined using a pointwise evaluation, namely $(\hat{\rho}\mathbf{v})^{n+1}_{m,i} = \hat{\rho}^{n+1}_{m,i}\hat{\mathbf{v}}^{n+1}_{m,i}$ (here, no summation over repeated indices is used). In order to ease the notation we introduce the following matrix and tensor definitions, according to [43,42]:

$$\mathbf{M}^+_j = \int\limits_{\mathbf{R}_j} \tilde{\psi}^{(j)}_k(\mathbf{x}, t^{n+1,-})\tilde{\psi}^{(j)}_m(\mathbf{x}, t^{n+1,-}) d\mathbf{x}, \qquad \bar{\mathbf{M}}^+_i = \int\limits_{\mathbf{T}_i} \tilde{\phi}^{(i)}_k(\mathbf{x}, t^{n+1,-})\tilde{\phi}^{(i)}_m(\mathbf{x}, t^{n+1,-}) d\mathbf{x}, \tag{16}$$

$$\mathbf{M}^-_j = \int\limits_{\mathbf{R}_j} \tilde{\psi}^{(j)}_k(\mathbf{x}, t^{n,+})\tilde{\psi}^{(j)}_m(\mathbf{x}, t^{n,-}) d\mathbf{x}, \qquad \bar{\mathbf{M}}^-_i = \int\limits_{\mathbf{T}_i} \tilde{\phi}^{(i)}_k(\mathbf{x}, t^{n,+})\tilde{\phi}^{(i)}_m(\mathbf{x}, t^{n,-}) d\mathbf{x}, \tag{17}$$

$$\mathbf{M}^\circ_j = \int\limits_{\mathbf{R}^{st}_j} \frac{\partial \tilde{\psi}^{(j)}_k}{\partial t} \tilde{\psi}^{(j)}_m d\mathbf{x}dt, \qquad \bar{\mathbf{M}}^\circ_i = \int\limits_{\mathbf{T}^{st}_i} \frac{\partial \tilde{\phi}^{(i)}_k}{\partial t} \tilde{\phi}^{(i)}_m d\mathbf{x}dt, \tag{18}$$

$$\mathbf{M}_j = \mathbf{M}^+_j - \mathbf{M}^\circ_j, \qquad \bar{\mathbf{M}}_i = \bar{\mathbf{M}}^+_i - \bar{\mathbf{M}}^\circ_i, \tag{19}$$

$$\mathbf{S}_j = \int\limits_{\mathbf{R}^{st}_j} \tilde{\psi}^{(j)}_k \mathbf{S}_\sigma d\mathbf{x}dt, \qquad (\rho\mathbf{S})_i = \int\limits_{\mathbf{T}^{st}_i} \tilde{\phi}^{(i)}_k \rho\mathbf{S}_v d\mathbf{x}dt \tag{20}$$

$$\mathcal{D}_{i,j} = \int\limits_{\Gamma^{st}_j} \tilde{\phi}^{(i)}_k \tilde{\psi}^{(j)}_m \mathbf{n}_{i,j} dSdt - \int\limits_{\mathbf{T}^{st}_{i,j}} \nabla\tilde{\phi}^{(i)}_k \tilde{\psi}^{(j)}_m d\mathbf{x}dt, \tag{21}$$

$$\mathcal{Q}_{i,j} = \int\limits_{\mathbf{T}^{st}_{i,j}} \tilde{\psi}^{(j)}_k \nabla\tilde{\phi}^{(i)}_m \tilde{\psi}^{(j)}_q d\mathbf{x}dt - \int\limits_{\Gamma^{st}_j} \tilde{\psi}^{(j)}_k \tilde{\phi}^{(i)}_m \tilde{\psi}^{(j)}_q s_{i,j}\mathbf{n}_j dSdt, \tag{22}$$

where $s_{i,j}$ is a sign function defined by

$$s_{i,j} = \frac{r(j) - 2i + \ell(j)}{r(j) - \ell(j)}. \tag{23}$$

Equations (14) and (15) are then rewritten in a compact form as

$$\bar{\mathbf{M}}_i(\hat{\rho}\mathbf{v})^{n+1}_i = \bar{\mathbf{M}}^-_i (\hat{\rho}\mathbf{v})^n_i + \sum_{j\in S_i} \mathcal{D}_{i,j} \cdot \hat{\boldsymbol{\sigma}}^{n+1}_j + (\rho\mathbf{S})_i, \tag{24}$$

$$\mathbf{M}_j\hat{\boldsymbol{\sigma}}^{n+1}_j = \mathbf{M}^-_j \hat{\boldsymbol{\sigma}}^n_j + \hat{\mathbf{E}}_j \cdot \mathcal{Q}_{\ell(j),j}\hat{\mathbf{v}}^{n+1}_{\ell(j)} + \hat{\mathbf{E}}_j \cdot \mathcal{Q}_{r(j),j}\hat{\mathbf{v}}^{n+1}_{r(j)} + \mathbf{S}_j. \tag{25}$$

Formal substitution of the discrete PDE for the stress tensor (25) into the discrete momentum equation (24), i.e. application of the Schur complement, yields a linear system that corresponds to a *discrete second order wave equation* for all degrees of freedom of the velocity vector field $\mathbf{v}_h$ and which reads

$$\bar{\mathbf{M}}_i \, \hat{\rho}_i\hat{\mathbf{v}}^{n+1}_i - \sum_{j\in S_i} \mathcal{D}_{i,j} \cdot \mathbf{M}^{-1}_j \left(\hat{\mathbf{E}}_j \cdot \mathcal{Q}_{\ell(j),j}\hat{\mathbf{v}}^{n+1}_{\ell(j)} + \hat{\mathbf{E}}_j \cdot \mathcal{Q}_{r(j),j}\hat{\mathbf{v}}^{n+1}_{r(j)} \right)$$

$$= \bar{\mathbf{M}}^-_i \, \hat{\rho}_i\hat{\mathbf{v}}^n_i + \sum_{j\in S_i} \mathcal{D}_{i,j} \cdot \mathbf{M}^{-1}_j \left(\mathbf{M}^-_j \hat{\boldsymbol{\sigma}}^n_j + \mathbf{S}_j \right) + (\rho\mathbf{S})_i. \tag{26}$$

The shape of this system can be rather complex if explicitly expressed in terms of all components of $\mathbf{v}_h$ and $\mathbf{E}_h$. For anisotropic materials, the system has exactly the same formal structure as given in (26), just with a more complex tensor $\hat{\mathbf{E}}_j$ compared to simple isotropic material. In any case, the system involves only the velocity field of the direct neighbors of each element and thus becomes a 4-point block system in two space dimensions and a 5-point block system in three space dimensions. For the particular case of $p_\gamma = 0$ (piecewise constant polynomials in time, i.e. $\mathbf{M}^\circ_j = \bar{\mathbf{M}}^\circ_i = 0$, $\mathbf{M}^+_j = \mathbf{M}^-_j = \mathbf{M}_j$, $\bar{\mathbf{M}}^+_i = \bar{\mathbf{M}}^-_i = \bar{\mathbf{M}}_i$), second order of accuracy in time can be easily achieved with the Crank–Nicolson scheme. In this setting, equations (24) and (25) read

$$\bar{\boldsymbol{M}}_i(\hat{\rho}\mathbf{v})_i^{n+1} = \bar{\boldsymbol{M}}_i(\hat{\rho}\mathbf{v})_i^n + \sum_{j\in S_i}\boldsymbol{\mathcal{D}}_{i,j}\cdot\hat{\boldsymbol{\sigma}}_j^{n+\frac{1}{2}} + (\rho\boldsymbol{\mathcal{S}})_i, \tag{27}$$

$$\boldsymbol{M}_j\hat{\boldsymbol{\sigma}}_j^{n+1} = \boldsymbol{M}_j\hat{\boldsymbol{\sigma}}_j^n + \hat{\mathbf{E}}_j\cdot\boldsymbol{\mathcal{Q}}_{\ell(j),j}\hat{\mathbf{v}}_{\ell(j)}^{n+\frac{1}{2}} + \hat{\mathbf{E}}_j\cdot\boldsymbol{\mathcal{Q}}_{r(j),j}\hat{\mathbf{v}}_{r(j)}^{n+\frac{1}{2}} + \boldsymbol{\mathcal{S}}_j, \tag{28}$$

with $\hat{\boldsymbol{\sigma}}_j^{n+\frac{1}{2}} = \frac{1}{2}\left(\hat{\boldsymbol{\sigma}}_j^n + \hat{\boldsymbol{\sigma}}_j^{n+1}\right)$ and $\hat{\mathbf{v}}_i^{n+\frac{1}{2}} = \frac{1}{2}\left(\hat{\mathbf{v}}_i^n + \hat{\mathbf{v}}_i^{n+1}\right)$. In this case the final velocity system reads

$$\bar{\boldsymbol{M}}_i\hat{\rho}_i\hat{\mathbf{v}}_i^{n+1} - \frac{1}{4}\sum_{j\in S_i}\boldsymbol{\mathcal{D}}_{i,j}\cdot\boldsymbol{M}_j^{-1}\left(\hat{\mathbf{E}}_j\cdot\boldsymbol{\mathcal{Q}}_{i,j}\hat{\mathbf{v}}_i^{n+1} + \hat{\mathbf{E}}_j\cdot\boldsymbol{\mathcal{Q}}_{\wp(i,j),j}\hat{\mathbf{v}}_{\wp(i,j)}^{n+1}\right) =$$

$$\bar{\boldsymbol{M}}_i\hat{\rho}_i\hat{\mathbf{v}}_i^n + \sum_{j\in S_i}\boldsymbol{\mathcal{D}}_{i,j}\cdot\left(\hat{\boldsymbol{\sigma}}_j^n + \frac{1}{2}\boldsymbol{M}_j^{-1}\boldsymbol{\mathcal{S}}_j\right) + \frac{1}{4}\sum_{j\in S_i}\boldsymbol{\mathcal{D}}_{i,j}\cdot\boldsymbol{M}_j^{-1}\left(\hat{\mathbf{E}}_j\cdot\boldsymbol{\mathcal{Q}}_{i,j}\hat{\mathbf{v}}_i^n + \hat{\mathbf{E}}_j\cdot\boldsymbol{\mathcal{Q}}_{\wp(i,j),j}\hat{\mathbf{v}}_{\wp(i,j)}^n\right) + (\rho\boldsymbol{\mathcal{S}})_i. \tag{29}$$

It can be shown to be symmetric and positive definite for homogeneous materials. The proof of those properties is reported in Section 5 for the homogeneous case. Thanks to those properties we are able, for this special choice, to use a very fast linear solver such as the conjugate gradient (CG) method. For $p_\gamma > 0$ the system is not symmetric anymore and since the time derivatives appear in both equations the symmetrization strategy adopted in [44] for the incompressible Navier–Stokes equations is not possible any more. In any case we can still solve the system using a matrix-free GMRES algorithm [84] in order to obtain the degrees of freedom $\hat{\mathbf{v}}_i^{n+1}$ of the velocity field at the new time slice. Once the new velocity field is known, we can then readily update the stress tensor at the aid of (25) for $p_\gamma > 0$ or via (28) for $p_\gamma = 0$. This closes the description of the numerical method, which is analyzed in the subsequent section.

5. Properties of the staggered space–time DG schemes for linear elasticity

In this section we report some details about the main matrix for the velocity system that needs to be solved in each time step, as well as some theoretical results about the energy stability of the numerical method.

5.1. Symmetry and positive definiteness for the special case of a Crank–Nicolson scheme in time

For homogeneous material ($\rho = const.$, $\mathbf{E} = const.$) and for $p_\gamma = 0$ combined with the Crank–Nicolson scheme in time, the linear system (29) reduces to

$$\rho\bar{\boldsymbol{M}}_i\hat{\mathbf{v}}_i^{n+1} - \frac{1}{4}\sum_{j\in S_i}\boldsymbol{\mathcal{D}}_{i,j}\cdot\boldsymbol{M}_j^{-1}\mathbf{E}\cdot\left(\tilde{\boldsymbol{\mathcal{Q}}}_{i,j}\cdot\hat{\mathbf{v}}_i^{n+1} + \tilde{\boldsymbol{\mathcal{Q}}}_{\wp(i,j),j}\cdot\hat{\mathbf{v}}_{\wp(i,j)}^{n+1}\right) = \mathbf{b}_i^n, \tag{30}$$

with the known right hand side $\mathbf{b}_i^n$ and the matrix

$$\tilde{\boldsymbol{\mathcal{Q}}}_{i,j} = \left(\tilde{Q}_{i,j}\right)_l^{\kappa\mu} = \int\limits_{\boldsymbol{T}_{i,j}^{st}}\tilde{\psi}_\kappa^{(j)}\partial_l\tilde{\phi}_\mu^{(i)}\,d\mathbf{x}dt - \int\limits_{\Gamma_j^{st}}\tilde{\psi}_\kappa^{(j)}\tilde{\phi}_\mu^{(i)}s_{i,j}(n_j)_l dSdt. \tag{31}$$

Note that the rank 3 tensor $\boldsymbol{\mathcal{Q}}_{i,j}$ can be simplified to $\tilde{\boldsymbol{\mathcal{Q}}}_{i,j}$ in the case of constant material properties. In this section, we use Greek upper indices for the basis and test functions in the objects $\tilde{\boldsymbol{\mathcal{Q}}}_{i,j}$ and $\boldsymbol{\mathcal{D}}_{i,j}$, and Latin lower indices for spatial vectors and tensors. The indices i and j are reserved for the numbers of the element and the face.

Theorem 1. *In the homogeneous isotropic case and for $p_\gamma = 0$, the matrix of system* (30) *is symmetric.*

Proof. Since the material is assumed to be homogeneous, ρ and $\mathbf{E}$ are constant in space and time. Due to the symmetry of the stress tensor $\sigma_{ij} = \sigma_{ji}$ and the strain tensor $\epsilon_{kl} = \epsilon_{lk}$, we also have $E_{ijkl} = E_{jikl} = E_{jilk}$, which are the so-called *minor symmetries* of $\mathbf{E}$. The so-called *major symmetries* of $\mathbf{E}$ imply also that $\mathbf{E}_{ijkl} = \mathbf{E}_{klij}$. All these symmetries of $\mathbf{E}$ are summarized in the shorthand notation $\mathbf{E} = \mathbf{E}^\top$. Furthermore, from the definitions (31) and (21) it is obvious to see that $\tilde{\boldsymbol{\mathcal{Q}}}_{i,j} = -\boldsymbol{\mathcal{D}}_{i,j}^\top$, see also [43]. From (16)–(19) one obtains that $\bar{\boldsymbol{M}}_i = \bar{\boldsymbol{M}}_i^\top$ for $p_\gamma = 0$. The diagonal block in (30) then reads

$$\mathbf{D}_i = \rho\bar{\boldsymbol{M}}_i + \frac{1}{4}\sum_{j\in S_i}\boldsymbol{\mathcal{D}}_{i,j}\boldsymbol{M}_j^{-1}\mathbf{E}\cdot\boldsymbol{\mathcal{D}}_{i,j}^\top, \tag{32}$$

or, more conveniently in index notation (Greek upper indices refer to basis and test functions, Latin lower indices to spatial vectors and tensors)

$$\mathbf{D}_i = (D_i)^{\mu\nu}_{kl} = \rho \left(\bar{M}_i \right)^{\mu\nu} \delta_{kl} + \frac{1}{4} \sum_{j \in S_i} \left(D_{i,j} \right)^{\mu\kappa}_p \left(\boldsymbol{M}_j^{-1} \right)^{\kappa\alpha} E_{kplm} \left(D_{i,j} \right)^{\nu\alpha}_m ,$$ (33)

and it is easy to see that its transpose verifies

$$\mathbf{D}_i^\top = \rho \bar{\boldsymbol{M}}_i^\top + \frac{1}{4} \sum_{j \in S_i} \boldsymbol{\mathcal{D}}_{i,j} \boldsymbol{M}_j^{-\top} \mathbf{E}^\top \cdot \boldsymbol{\mathcal{D}}_{i,j}^\top = \mathbf{D}_i,$$ (34)

or, more conveniently in index notation

$$\mathbf{D}_i^\top = (D_i)^{\nu\mu}_{lk} = \rho \left(\bar{M}_i \right)^{\nu\mu} \delta_{lk} + \frac{1}{4} \sum_{j \in S_i} \left(D_{i,j} \right)^{\nu\kappa}_p \left(\boldsymbol{M}_j^{-1} \right)^{\kappa\alpha} E_{lpkm} \left(D_{i,j} \right)^{\mu\alpha}_m =$$

$$= \rho \left(\bar{M}_i \right)^{\mu\nu} \delta_{kl} + \frac{1}{4} \sum_{j \in S_i} \left(D_{i,j} \right)^{\mu\alpha}_m \left(\boldsymbol{M}_j^{-1} \right)^{\alpha\kappa} E_{kmlp} \left(D_{i,j} \right)^{\nu\kappa}_p = (D_i)^{\mu\nu}_{kl} = \mathbf{D}_i,$$ (35)

where we have used the major symmetry of E_{ijkl}, the symmetries of the mass matrix and of the Kronecker delta δ_{kl} and the simple renaming of contracted indices.

The off-diagonal blocks involving the neighbor elements $\wp(i,j)$ of element i read

$$\mathbf{N}_{i,\wp(i,j)} = -\frac{1}{4} \boldsymbol{\mathcal{D}}_{i,j} \boldsymbol{M}_j^{-1} \mathbf{E} \cdot \tilde{\boldsymbol{\mathcal{Q}}}_{\wp(i,j),j} = \frac{1}{4} \boldsymbol{\mathcal{D}}_{i,j} \boldsymbol{M}_j^{-1} \mathbf{E} \cdot \boldsymbol{\mathcal{D}}_{\wp(i,j),j}^\top.$$ (36)

We write now the previous contribution in terms of edges $j \in [1, N_j]$ so that $\mathbf{N}_{\ell(j),r(j)}$ and $\mathbf{N}_{r(j),\ell(j)}$ are the off-diagonal blocks involving the contribution of $r(j)$ to $\ell(j)$ and vice-versa. So we have to show that $\mathbf{N}_{\ell(j),r(j)} = \mathbf{N}_{r(j),\ell(j)}^\top$, but

$$\mathbf{N}_{r(j),\ell(j)}^\top = \frac{1}{4} \left(\boldsymbol{\mathcal{D}}_{r(j),j} \boldsymbol{M}_j^{-1} \mathbf{E} \cdot \boldsymbol{\mathcal{D}}_{\ell(j),j}^\top \right)^\top = \frac{1}{4} \boldsymbol{\mathcal{D}}_{\ell(j),j} \boldsymbol{M}_j^{-\top} \mathbf{E}^\top \boldsymbol{\mathcal{D}}_{r(j),j}^\top = \mathbf{N}_{\ell(j),r(j)},$$ (37)

or, using again the index notation,

$$\mathbf{N}_{r(j),\ell(j)}^\top = \left(N_{r(j),\ell(j)} \right)^{\nu\mu}_{lk} = \frac{1}{4} \left(D_{r(j),j} \right)^{\nu\kappa}_p \left(\boldsymbol{M}_j^{-1} \right)^{\kappa\alpha} E_{lpkm} \left(D_{\ell(j),j} \right)^{\mu\alpha}_m =$$

$$= \frac{1}{4} \left(D_{\ell(j),j} \right)^{\mu\alpha}_m \left(\boldsymbol{M}_j^{-1} \right)^{\alpha\kappa} E_{kmlp} \left(D_{r(j),j} \right)^{\nu\kappa}_p = \left(N_{\ell(j),r(j)} \right)^{\mu\nu}_{kl} = \mathbf{N}_{\ell(j),r(j)}$$ (38)

from the symmetries of $\mathbf{E}$ and $\boldsymbol{M}_j$. □

Theorem 2. *In the homogeneous case and $p_\gamma = 0$, the matrix of system* (30) *is positive definite.*

Proof. We can follow the same reasoning as in [78], since $\bar{M}_i = \bar{M}_i^\top > 0$ and $\mathbf{E} = \mathbf{E}^\top > 0$. With these properties and from the results of [78] we obtain that the system matrix of (30) without the term $\rho \boldsymbol{M}_i$ is at least positive semi-definite. If we add the contribution of the positive definite mass matrix $\rho \bar{\boldsymbol{M}}_i > 0$, then the resulting system matrix in (30) is positive definite. □

Numerical evidence shows that also the non-homogeneous case seems to have the same properties, but unfortunately a rigorous mathematical proof is still missing for the general non-homogeneous case.

5.2. Stability analysis

In this section we prove some stability results for the proposed scheme in the energy norm. In particular we will demonstrate that the semi-discrete scheme is *energy preserving* and that the fully discrete staggered space–time DG scheme is *energy stable*. A particular case is given by $p_\gamma = 0$ combined with the Crank–Nicolson time discretization, for which the fully discrete scheme is *exactly energy preserving*.

Theorem 3. *For homogeneous material with $\rho > 0$, $\mathbf{E} = \mathbf{E}^\top > 0$ and in the absence of volume source terms the semi-discrete form of the proposed staggered DG scheme is energy preserving.*

Proof. Since $\mathbf{E} = \mathbf{E}^\top > 0$ one also has $\mathbf{E}^{-1} = \mathbf{E}^{-\top} > 0$. The semi-discrete form of the scheme with no volume source terms is given by

$$\int_{\boldsymbol{T}_i} \phi^{(i)} \frac{\partial (\rho \mathbf{v})_i}{\partial t} d\mathbf{x} = \sum_{j \in S_i} \left(\int_{\Gamma_j} \phi^{(i)} \boldsymbol{\sigma}_j \cdot \mathbf{n}_{i,j} dS - \int_{\boldsymbol{T}_{i,j}} \nabla \phi^{(i)} \boldsymbol{\sigma}_j d\mathbf{x} \right),$$ (39)

$$\int\limits_{\boldsymbol{R}_j} \psi^{(j)} \frac{\partial \boldsymbol{\sigma}_j}{\partial t} d\mathbf{x} = \int\limits_{\boldsymbol{T}_{\ell(j),j}} \psi^{(j)} \mathbf{E}_j \cdot \nabla \mathbf{v}_{\ell(j)} d\mathbf{x} + \int\limits_{\boldsymbol{T}_{r(j),j}} \psi^{(j)} \mathbf{E}_j \cdot \nabla \mathbf{v}_{r(j)} d\mathbf{x} + \int\limits_{\Gamma_j} \psi^{(j)} \mathbf{E}_j \cdot \left(\mathbf{v}_{r(j)} - \mathbf{v}_{\ell(j)}\right) \otimes \mathbf{n}_j dS. \tag{40}$$

Since the material is assumed to be homogeneous, we can take $\psi^{(j)} = \mathbf{E}_j^{-1} \cdot \boldsymbol{\sigma}_j$ and $\phi^{(i)} = \mathbf{v}_i$ as test functions, sum up all contributions (we use the index contraction $\boldsymbol{\sigma} : \boldsymbol{B} = \sigma_{ij} B_{ij}$ and the identity $\mathbf{E}^{-1} \cdot \boldsymbol{\sigma} : \mathbf{E} \cdot \boldsymbol{B} = E_{ijmn}^{-1} \sigma_{mn} E_{ijkl} B_{kl} = E_{mnij}^{-1} E_{ijkl} \sigma_{mn} B_{kl} = \delta_{mnkl} \sigma_{mn} B_{kl} = \sigma_{kl} B_{kl} = \boldsymbol{\sigma} : \boldsymbol{B}$) and thus obtain the two *scalar* relations

$$\int\limits_{\boldsymbol{T}_i} \mathbf{v}_i \cdot \frac{\partial (\rho \mathbf{v})_i}{\partial t} d\mathbf{x} = \sum_{j \in S_i} \left(\int\limits_{\Gamma_j} \mathbf{v}_i \cdot \left(\boldsymbol{\sigma}_j \cdot \mathbf{n}_{i,j}\right) dS - \int\limits_{\boldsymbol{T}_{i,j}} \nabla \mathbf{v}_i : \boldsymbol{\sigma}_j d\mathbf{x} \right), \tag{41}$$

$$\int\limits_{\boldsymbol{R}_j} \left(\mathbf{E}_j^{-1} \cdot \boldsymbol{\sigma}_j \right) : \frac{\partial \boldsymbol{\sigma}_j}{\partial t} d\mathbf{x} = \int\limits_{\boldsymbol{T}_{\ell(j),j}} \boldsymbol{\sigma}_j : \nabla \mathbf{v}_{\ell(j)} d\mathbf{x} + \int\limits_{\boldsymbol{T}_{r(j),j}} \boldsymbol{\sigma}_j : \nabla \mathbf{v}_{r(j)} d\mathbf{x} + \int\limits_{\Gamma_j} \boldsymbol{\sigma}_j : \left(\mathbf{v}_{r(j)} - \mathbf{v}_{\ell(j)}\right) \otimes \mathbf{n}_j dS. \tag{42}$$

Summing over the entire domain yields

$$\sum_{i=1}^{N_i} \int\limits_{\boldsymbol{T}_i} \mathbf{v}_i \cdot \frac{\partial (\rho \mathbf{v})_i}{\partial t} d\mathbf{x} = \sum_{i=1}^{N_i} \sum_{j \in S_i} \left(\int\limits_{\Gamma_j} \mathbf{v}_i \cdot \left(\boldsymbol{\sigma}_j \cdot \mathbf{n}_{i,j}\right) dS - \int\limits_{\boldsymbol{T}_{i,j}} \nabla \mathbf{v}_i : \boldsymbol{\sigma}_j d\mathbf{x} \right), \tag{43}$$

$$\sum_{j=1}^{N_j} \int\limits_{\boldsymbol{R}_j} \left(\mathbf{E}_j^{-1} \cdot \boldsymbol{\sigma}_j \right) : \frac{\partial \boldsymbol{\sigma}_j}{\partial t} d\mathbf{x} = \sum_{j=1}^{N_j} \left(\int\limits_{\boldsymbol{T}_{\ell(j),j}} \boldsymbol{\sigma}_j : \nabla \mathbf{v}_{\ell(j)} d\mathbf{x} + \int\limits_{\boldsymbol{T}_{r(j),j}} \boldsymbol{\sigma}_j : \nabla \mathbf{v}_{r(j)} d\mathbf{x} + \int\limits_{\Gamma_j} \boldsymbol{\sigma}_j : \left(\mathbf{v}_{r(j)} - \mathbf{v}_{\ell(j)}\right) \otimes \mathbf{n}_j dS \right). \tag{44}$$

With $\boldsymbol{\sigma} = \boldsymbol{\sigma}^\top$, $\mathbf{E} = \mathbf{E}^\top$ and therefore $\mathbf{E}^{-1} = \mathbf{E}^{-\top}$ we can rewrite the time derivative terms as

$$\sum_{i=1}^{N_i} \int\limits_{\boldsymbol{T}_i} \mathbf{v}_i \cdot \frac{\partial (\rho \mathbf{v})_i}{\partial t} d\mathbf{x} = \frac{1}{2} \int\limits_{\Omega} \frac{\partial \rho_h \mathbf{v}_h^2}{\partial t} d\mathbf{x}, \tag{45}$$

$$\sum_{j=1}^{N_j} \int\limits_{\boldsymbol{R}_j} \left(\mathbf{E}_j^{-1} \cdot \boldsymbol{\sigma}_j \right) : \frac{\partial \boldsymbol{\sigma}_j}{\partial t} d\mathbf{x} = \frac{1}{2} \int\limits_{\Omega} \frac{\partial}{\partial t} \left(\boldsymbol{\sigma}_h : \mathbf{E}_h^{-1} \cdot \boldsymbol{\sigma}_h \right) d\mathbf{x}, \tag{46}$$

and since $\boldsymbol{\sigma}_j$ is continuous across Γ_j the right hand side of (43) can be written in terms of the faces Γ_j as

$$\sum_{i=1}^{N_i} \sum_{j \in S_i} \left(\int\limits_{\Gamma_j} \mathbf{v}_i \cdot \left(\boldsymbol{\sigma}_j \cdot \mathbf{n}_{i,j}\right) dS - \int\limits_{\boldsymbol{T}_{i,j}} \nabla \mathbf{v}_i : \boldsymbol{\sigma}_j d\mathbf{x} \right) = \sum_{j=1}^{N_j} \left(\int\limits_{\Gamma_j} \boldsymbol{\sigma}_j : \left(\mathbf{v}_{\ell(j)} - \mathbf{v}_{r(j)}\right) \otimes \mathbf{n}_j dS \right.$$

$$\left. - \int\limits_{\boldsymbol{T}_{r(j),j}} \nabla \mathbf{v}_{r(j)} : \boldsymbol{\sigma}_j d\mathbf{x} dt - \int\limits_{\boldsymbol{T}_{\ell(j),j}} \nabla \mathbf{v}_{\ell(j)} : \boldsymbol{\sigma}_j d\mathbf{x} \right). \tag{47}$$

Summing Eqs. (43)–(44) and making use of Eqs. (45) and (46) and since the right hand sides of (43) and (44) add up to zero due to (47), one finally obtains

$$\frac{1}{2} \int\limits_{\Omega} \frac{\partial}{\partial t} \left(\boldsymbol{\sigma}_h : \mathbf{E}_h^{-1} \cdot \boldsymbol{\sigma}_h + \rho_h \mathbf{v}_h^2 \right) d\mathbf{x} = 0. \tag{48}$$

This means that the total energy, which is the sum of the kinetic energy and the mechanical energy, is conserved for the semi-discrete scheme. □

We show now similar results for the fully discrete forms. The first result can be seen as a simple extension of the previous theorem using the ideas presented in [85,42].

Theorem 4. *For homogeneous material with $\rho > 0$, $\mathbf{E} = \mathbf{E}^\top > 0$ and in the absence of volume source terms, the staggered space–time DG scheme* (11) *and* (12) *with* (13) *is energy stable for $p_\gamma \geq 0$ for arbitrary meshes and for arbitrary time step size Δt.*

Proof. The fully-discrete staggered space–time DG method (11) and (12) with (13) in the absence of volume source terms reads

$$
\int_{T_i} \rho_i \tilde{\phi}^{(i)}(\mathbf{x}, t^{n+1,-}) \mathbf{v}_i(\mathbf{x}, t^{n+1,-}) d\mathbf{x} - \int_{T_i} \rho_i \tilde{\phi}^{(i)}(\mathbf{x}, t^{n,+}) \mathbf{v}_i(\mathbf{x}, t^{n,-}) d\mathbf{x} - \int_{T_i^{st}} \rho_i \frac{\partial \tilde{\phi}^{(i)}}{\partial t} \mathbf{v}_i d\mathbf{x} dt =
$$

$$
\sum_{j \in S_i} \left(\int_{\Gamma_j^{st}} \tilde{\phi}^{(i)} \boldsymbol{\sigma}_j \cdot \mathbf{n}_{i,j} dS\, dt - \int_{T_{i,j}^{st}} \nabla \tilde{\phi}^{(i)} \boldsymbol{\sigma}_j d\mathbf{x} dt \right), \tag{49}
$$

$$
\int_{R_j} \tilde{\psi}^{(i)}(\mathbf{x}, t^{n+1,-}) \boldsymbol{\sigma}_j(\mathbf{x}, t^{n+1,-}) d\mathbf{x} - \int_{R_j} \tilde{\psi}^{(i)}(\mathbf{x}, t^{n,+}) \boldsymbol{\sigma}_j(\mathbf{x}, t^{n,-}) d\mathbf{x} - \int_{R_j^{st}} \frac{\partial \tilde{\psi}^{(i)}}{\partial t} \boldsymbol{\sigma}_j d\mathbf{x} dt =
$$

$$
\int_{T_{\ell(j),j}^{st}} \tilde{\psi}^{(j)} \mathbf{E}_j \cdot \nabla \mathbf{v}_{\ell(j)} d\mathbf{x} dt + \int_{T_{r(j),j}^{st}} \tilde{\psi}^{(j)} \mathbf{E}_j \cdot \nabla \mathbf{v}_{r(j)} d\mathbf{x} dt + \int_{\Gamma_j^{st}} \tilde{\psi}^{(j)} \mathbf{E}_j \cdot (\mathbf{v}_{r(j)} - \mathbf{v}_{\ell(j)}) \otimes \mathbf{n}_j dS\, dt. \tag{50}
$$

Taking $\tilde{\psi}^{(j)} = \mathbf{E}_j^{-1} \cdot \boldsymbol{\sigma}_j$ and $\tilde{\phi}^{(i)} = \mathbf{v}_i$ as test functions, summing up all contributions and proceeding in the same manner as in the proof of the previous theorem, we arrive at the following intermediate scalar expression (also here the right hand side terms add again up to zero, for the same reason as before):

$$
\int_{\Omega} \rho_h \mathbf{v}_h(\mathbf{x}, t^{n+1,-}) \cdot \mathbf{v}_h(\mathbf{x}, t^{n+1,-}) d\mathbf{x} - \int_{\Omega} \rho_h \mathbf{v}_h(\mathbf{x}, t^{n,+}) \cdot \mathbf{v}_h(\mathbf{x}, t^{n,-}) d\mathbf{x} - \frac{1}{2} \int_{t^n}^{t^{n+1}} \int_{\Omega} \frac{\partial \rho_h \mathbf{v}_h^2}{\partial t} d\mathbf{x} dt +
$$

$$
\int_{\Omega} \boldsymbol{\sigma}_h(\mathbf{x}, t^{n+1,-}) : \mathbf{E}_h^{-1} \cdot \boldsymbol{\sigma}_h(\mathbf{x}, t^{n+1,-}) d\mathbf{x} - \int_{\Omega} \boldsymbol{\sigma}_h(\mathbf{x}, t^{n,-}) : \mathbf{E}_h^{-1} \cdot \boldsymbol{\sigma}_h(\mathbf{x}, t^{n,+}) d\mathbf{x} - \frac{1}{2} \int_{t^n}^{t^{n+1}} \int_{\Omega} \frac{\partial}{\partial t} \left(\boldsymbol{\sigma}_h : \mathbf{E}_h^{-1} \cdot \boldsymbol{\sigma}_h \right) d\mathbf{x} dt
$$

$$
= 0.
$$

The terms containing the time derivatives can be integrated by parts in time and thus one obtains:

$$
\frac{1}{2} \int_{\Omega} \rho_h \mathbf{v}_h^2(\mathbf{x}, t^{n+1,-}) d\mathbf{x} - \int_{\Omega} \rho_h \mathbf{v}_h(\mathbf{x}, t^{n,+}) \cdot \mathbf{v}_h(\mathbf{x}, t^{n,-}) d\mathbf{x} + \frac{1}{2} \int_{\Omega} \rho_h \mathbf{v}_h^2(\mathbf{x}, t^{n,+}) d\mathbf{x} +
$$

$$
\frac{1}{2} \int_{\Omega} \boldsymbol{\sigma}_h(\mathbf{x}, t^{n+1,-}) : \mathbf{E}_h^{-1} \cdot \boldsymbol{\sigma}_h(\mathbf{x}, t^{n+1,-}) d\mathbf{x} - \int_{\Omega} \boldsymbol{\sigma}_h(\mathbf{x}, t^{n,-}) : \mathbf{E}_h^{-1} \cdot \boldsymbol{\sigma}_h(\mathbf{x}, t^{n,+}) d\mathbf{x}
$$

$$
+ \frac{1}{2} \int_{\Omega} \boldsymbol{\sigma}_h(\mathbf{x}, t^{n,+}) : \mathbf{E}_h^{-1} \cdot \boldsymbol{\sigma}_h(\mathbf{x}, t^{n,+}) d\mathbf{x} = 0.
$$

Adding and immediately subtracting again $\frac{1}{2} \int_{\Omega} \rho_h \mathbf{v}_h^2(\mathbf{x}, t^{n,-}) d\mathbf{x}$ and $\frac{1}{2} \int_{\Omega} \boldsymbol{\sigma}_h(\mathbf{x}, t^{n,-}) : \mathbf{E}_h^{-1} \cdot \boldsymbol{\sigma}_h(\mathbf{x}, t^{n,-}) d\mathbf{x}$ yields

$$
\frac{1}{2} \int_{\Omega} \left(\rho_h \mathbf{v}_h^2(\mathbf{x}, t^{n+1,-}) + \boldsymbol{\sigma}_h(\mathbf{x}, t^{n+1,-}) : \mathbf{E}_h^{-1} \cdot \boldsymbol{\sigma}_h(\mathbf{x}, t^{n+1,-}) \right) d\mathbf{x}
$$

$$
- \frac{1}{2} \int_{\Omega} \left(\rho_h \mathbf{v}_h^2(\mathbf{x}, t^{n,-}) + \boldsymbol{\sigma}_h(\mathbf{x}, t^{n,-}) : \mathbf{E}_h^{-1} \cdot \boldsymbol{\sigma}_h(\mathbf{x}, t^{n,-}) \right) d\mathbf{x}
$$

$$
+ \frac{1}{2} \int_{\Omega} \rho_h \mathbf{v}_h^2(\mathbf{x}, t^{n,-}) d\mathbf{x} - \int_{\Omega} \rho_h \mathbf{v}_h(\mathbf{x}, t^{n,+}) \cdot \mathbf{v}_h(\mathbf{x}, t^{n,-}) d\mathbf{x} + \frac{1}{2} \int_{\Omega} \rho_h \mathbf{v}_h^2(\mathbf{x}, t^{n,+}) d\mathbf{x} +
$$

$$
+ \frac{1}{2} \int_{\Omega} \boldsymbol{\sigma}_h(\mathbf{x}, t^{n,-}) : \mathbf{E}_h^{-1} \cdot \boldsymbol{\sigma}_h(\mathbf{x}, t^{n,-}) d\mathbf{x} - \int_{\Omega} \boldsymbol{\sigma}_h(\mathbf{x}, t^{n,-}) : \mathbf{E}_h^{-1} \cdot \boldsymbol{\sigma}_h(\mathbf{x}, t^{n,+}) d\mathbf{x}
$$

$$
+ \frac{1}{2} \int_{\Omega} \boldsymbol{\sigma}_h(\mathbf{x}, t^{n,+}) : \mathbf{E}_h^{-1} \cdot \boldsymbol{\sigma}_h(\mathbf{x}, t^{n,+}) d\mathbf{x} = 0.
$$

The quadratic forms in the expressions above can be easily recognized, hence

$$\frac{1}{2}\int_\Omega \left(\rho_h \mathbf{v}_h^2(\mathbf{x}, t^{n+1,-}) + \boldsymbol{\sigma}_h(\mathbf{x}, t^{n+1,-}) : \mathbf{E}_h^{-1} \cdot \boldsymbol{\sigma}_h(\mathbf{x}, t^{n+1,-})\right) d\mathbf{x}$$

$$-\frac{1}{2}\int_\Omega \left(\rho_h \mathbf{v}_h^2(\mathbf{x}, t^{n,-}) + \boldsymbol{\sigma}_h(\mathbf{x}, t^{n,-}) : \mathbf{E}_h^{-1} \cdot \boldsymbol{\sigma}_h(\mathbf{x}, t^{n,-})\right) d\mathbf{x}$$

$$+\frac{1}{2}\int_\Omega \rho_h \left(\mathbf{v}_h(\mathbf{x}, t^{n,+}) - \mathbf{v}_h(\mathbf{x}, t^{n,-})\right)^2 d\mathbf{x} + \frac{1}{2}\int_\Omega \left(\boldsymbol{\sigma}_h(\mathbf{x}, t^{n,+}) - \boldsymbol{\sigma}_h(\mathbf{x}, t^{n,-})\right) : \mathbf{E}_h^{-1} \cdot \left(\boldsymbol{\sigma}_h(\mathbf{x}, t^{n,+}) - \boldsymbol{\sigma}_h(\mathbf{x}, t^{n,-})\right) d\mathbf{x}$$

$$= 0. \tag{51}$$

Since $\rho_h > 0$ and $\mathbf{E}_h > 0$ and thus the jump terms at time t^n are non-negative,

$$\frac{1}{2}\int_\Omega \rho_h \left(\mathbf{v}_h(\mathbf{x}, t^{n,+}) - \mathbf{v}_h(\mathbf{x}, t^{n,-})\right)^2 d\mathbf{x} + \frac{1}{2}\int_\Omega \left(\boldsymbol{\sigma}_h(\mathbf{x}, t^{n,+}) - \boldsymbol{\sigma}_h(\mathbf{x}, t^{n,-})\right) : \mathbf{E}_h^{-1} \cdot \left(\boldsymbol{\sigma}_h(\mathbf{x}, t^{n,+}) - \boldsymbol{\sigma}_h(\mathbf{x}, t^{n,-})\right) \geq 0, \tag{52}$$

we finally obtain from (51) and (52) the sought result which relates the total energy at the new time level with the total energy at the old time level as

$$\frac{1}{2}\int_\Omega \left(\rho_h \mathbf{v}_h^2(\mathbf{x}, t^{n+1,-}) + \boldsymbol{\sigma}_h(\mathbf{x}, t^{n+1,-}) : \mathbf{E}_h^{-1} \cdot \boldsymbol{\sigma}_h(\mathbf{x}, t^{n+1,-})\right) d\mathbf{x}$$

$$\leq \frac{1}{2}\int_\Omega \left(\rho_h \mathbf{v}_h^2(\mathbf{x}, t^{n,-}) + \boldsymbol{\sigma}_h(\mathbf{x}, t^{n,-}) : \mathbf{E}_h^{-1} \cdot \boldsymbol{\sigma}_h(\mathbf{x}, t^{n,-})\right) d\mathbf{x}, \tag{53}$$

from which we can conclude that our new staggered space–time DG scheme for the linear elasticity equations is *energy stable* for arbitrary polynomial approximation degree, general meshes and arbitrary time step size Δt. □

The previous theorem shows that the method is energy stable and that the rate of energy loss is proportional to the jump in the discrete solution at the interface between two time slices. This rises the almost natural question on what happens if we employ a second order time discretization using the classical Crank–Nicolson scheme. The following theorem gives us an interesting result:

Theorem 5. *For homogeneous material with $\rho > 0$, $\mathbf{E} = \mathbf{E}^\top > 0$ and in the absence of volume source terms the fully-discrete staggered DG scheme with $p_\gamma = 0$ and Crank–Nicolson time discretization is exactly energy preserving.*

Proof. Starting from the semi-discrete form (39) and (40), inserting the standard Crank–Nicolson time discretization and using as test functions $\psi^{(j)} = \mathbf{E}_j^{-1} \cdot \boldsymbol{\sigma}_j^{n+\frac{1}{2}}$ and $\phi^{(i)} = \mathbf{v}_j^{n+\frac{1}{2}}$, one obtains

$$\int_{\mathbf{T}_i} \rho_i \mathbf{v}_i^{n+\frac{1}{2}} \cdot \frac{\mathbf{v}_i^{n+1} - \mathbf{v}_i^n}{\Delta t} d\mathbf{x} = \sum_{j \in S_i} \left(\int_{\Gamma_j} \mathbf{v}_i^{n+\frac{1}{2}} \cdot \boldsymbol{\sigma}_j^{n+\frac{1}{2}} \cdot \mathbf{n}_{i,j} dS - \int_{\mathbf{T}_{i,j}} \nabla \mathbf{v}_i^{n+\frac{1}{2}} \cdot \boldsymbol{\sigma}_j^{n+\frac{1}{2}} d\mathbf{x}\right),$$

$$\int_{\mathbf{R}_j} \mathbf{E}_j^{-1} \cdot \boldsymbol{\sigma}_j^{n+\frac{1}{2}} : \frac{\boldsymbol{\sigma}_j^{n+1} - \boldsymbol{\sigma}_j^n}{\Delta t} d\mathbf{x} = \int_{\mathbf{T}_{\ell(j),j}} \boldsymbol{\sigma}_j^{n+\frac{1}{2}} : \nabla \mathbf{v}_{\ell(j)}^{n+\frac{1}{2}} d\mathbf{x} + \int_{\mathbf{T}_{r(j),j}} \boldsymbol{\sigma}_j^{n+\frac{1}{2}} : \nabla \mathbf{v}_{r(j)}^{n+\frac{1}{2}} d\mathbf{x}$$

$$+ \int_{\Gamma_j} \boldsymbol{\sigma}_j^{n+\frac{1}{2}} : (\mathbf{v}_{r(j)}^{n+\frac{1}{2}} - \mathbf{v}_{\ell(j)}^{n+\frac{1}{2}}) \otimes \mathbf{n}_j dS. \tag{54}$$

The right hand sides add again up to zero from the proof of Theorem 3, while for the discrete time derivatives we get from the definition of $\boldsymbol{\sigma}_j^{n+\frac{1}{2}} = \frac{1}{2}\left(\boldsymbol{\sigma}_j^n + \boldsymbol{\sigma}_j^{n+1}\right)$ and $\mathbf{v}_i^{n+\frac{1}{2}} = \frac{1}{2}\left(\mathbf{v}_i^n + \mathbf{v}_i^{n+1}\right)$ that

$$\int_\Omega \rho_h \mathbf{v}_h^{n+\frac{1}{2}} \frac{\mathbf{v}_h^{n+1} - \mathbf{v}_h^n}{\Delta t} d\mathbf{x} = \frac{1}{\Delta t} \frac{1}{2} \int_\Omega \rho_h \left(\left(\mathbf{v}_h^{n+1}\right)^2 - \left(\mathbf{v}_h^n\right)^2\right) d\mathbf{x}, \tag{55}$$
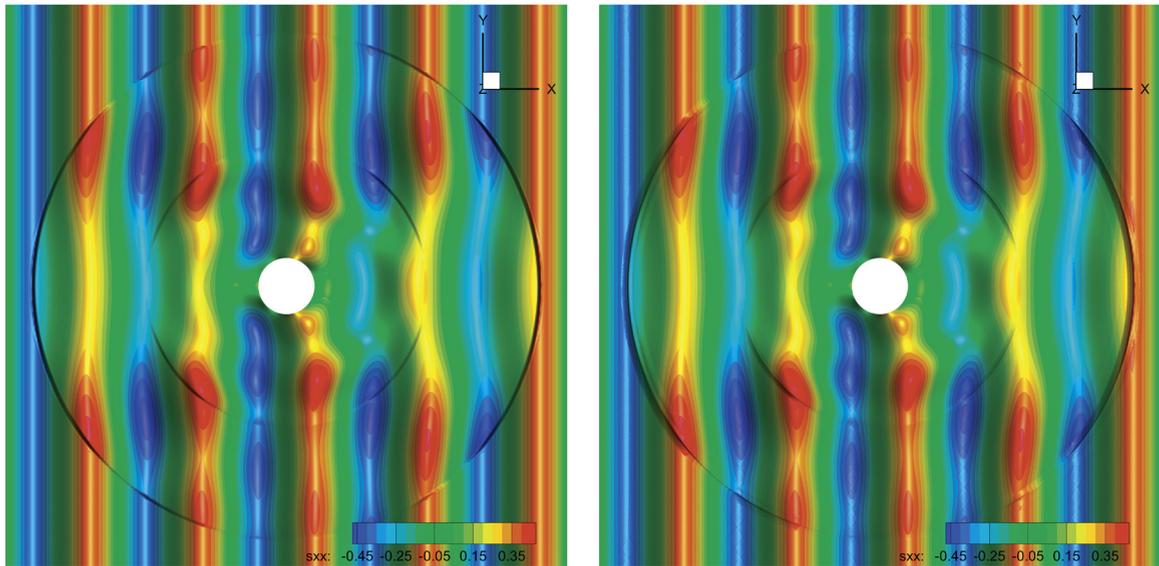
Fig. 3. Plane wave scattering on a circular cavity. Comparison of the isocontours of the stress tensor component σ_{xx} between the reference solution given by an explicit ADER-DG scheme (left) and our new staggered space–time DG scheme (right). (For interpretation of the colors in the figure(s), the reader is referred to the web version of this article.)

and a similar result for $\boldsymbol{\sigma}$. Using the same reasoning of Theorem (3) we finally obtain

$$\frac{1}{2}\int_{\Omega}\left(\rho_h\left(\mathbf{v}_h^{n+1}\right)^2+\boldsymbol{\sigma}_h^{n+1}:\mathbf{E}_j^{-1}\cdot\boldsymbol{\sigma}_h^{n+1}\right)d\mathbf{x}=\frac{1}{2}\int_{\Omega}\left(\rho_h\left(\mathbf{v}_h^n\right)^2+\boldsymbol{\sigma}_h^n:\mathbf{E}_j^{-1}\cdot\boldsymbol{\sigma}_h^n\right)d\mathbf{x}, \tag{56}$$

and so the staggered DG scheme with the simple Crank–Nicolson time discretization is *exactly energy preserving*. □

6. Numerical tests

All test problems in this section assume isotropic material. For the definition of the initial conditions, we also make use of the state vector $\mathbf{U}=\left(\sigma_{xx},\sigma_{yy},\sigma_{xy},u,v\right)$ in 2D and $\mathbf{U}=\left(\sigma_{xx},\sigma_{yy},\sigma_{zz},\sigma_{xy},\sigma_{yz},\sigma_{xz},u,v,w\right)$ in 3D.

6.1. Scattering of a plane wave on a circular cavity

In this test case we consider a simple p-wave traveling in the x-direction and hitting a circular cavity. The computational domain is $\Omega=[-2.5,2.5]^2-C_{0.25}$, where C_r indicates the circle of radius r. The initial condition is

$$\mathbf{U}(\mathbf{x},0)=0.1\cdot(-2,0,4,2,0)\sin(2\pi x), \tag{57}$$

and the boundary conditions are set to be periodic on the external boundary and free surface boundary ($\boldsymbol{\sigma}\cdot\mathbf{n}=0$) on the circular cavity. The material parameters are homogeneous and are chosen as $\rho=1$, $\lambda=2$ and $\mu=1$. The computational domain is discretized using $N_i=5644$ triangles of characteristic mesh size $h=0.11$. We use a polynomial approximation degree of $p=5$ in space and $p_\gamma=1$ in time. The time step size is chosen as $\Delta t=0.01$. We compare our new staggered space–time DG scheme with a well established explicit high order ADER-DG method that is the basis of the SeisSol code published in [27–31,86,87] and its generalization under the framework of $P_N P_M$ schemes achieved in [88]. For the reference solution, we use $N=M=2$ and a very fine mesh of $N_i=563280$ triangular elements. In both cases we run the simulation up to $t_{end}=1.0$. A comparison of the resulting stress component σ_{xx}, colored with σ_{yy} is shown in Fig. 3. Fig. 4 shows the time series of all variables in $\mathbf{x}_1=(0.5,0.5)$ and $\mathbf{x}_2=(1.0,0.0)$. A very good agreement can be observed in all cases. Furthermore, we emphasize that the use of high order isoparametric elements is important for properly representing the curvilinear geometry of this test case.

6.2. Numerical convergence test

In this test we verify the order of accuracy and the computational efficiency of our new staggered space–time DG schemes for linear elasticity. Following [27] we consider a combination of a p- and an s-wave in a square domain $\Omega=[-1.5,1.5]^2$ extended with periodic boundaries everywhere. As initial state we take

$$\mathbf{U}(\mathbf{x},0)=\alpha\mathbf{r}_p\sin(k\cdot\mathbf{x})+\alpha\mathbf{r}_s\sin(\mathbf{k}\cdot\mathbf{x}), \tag{58}$$

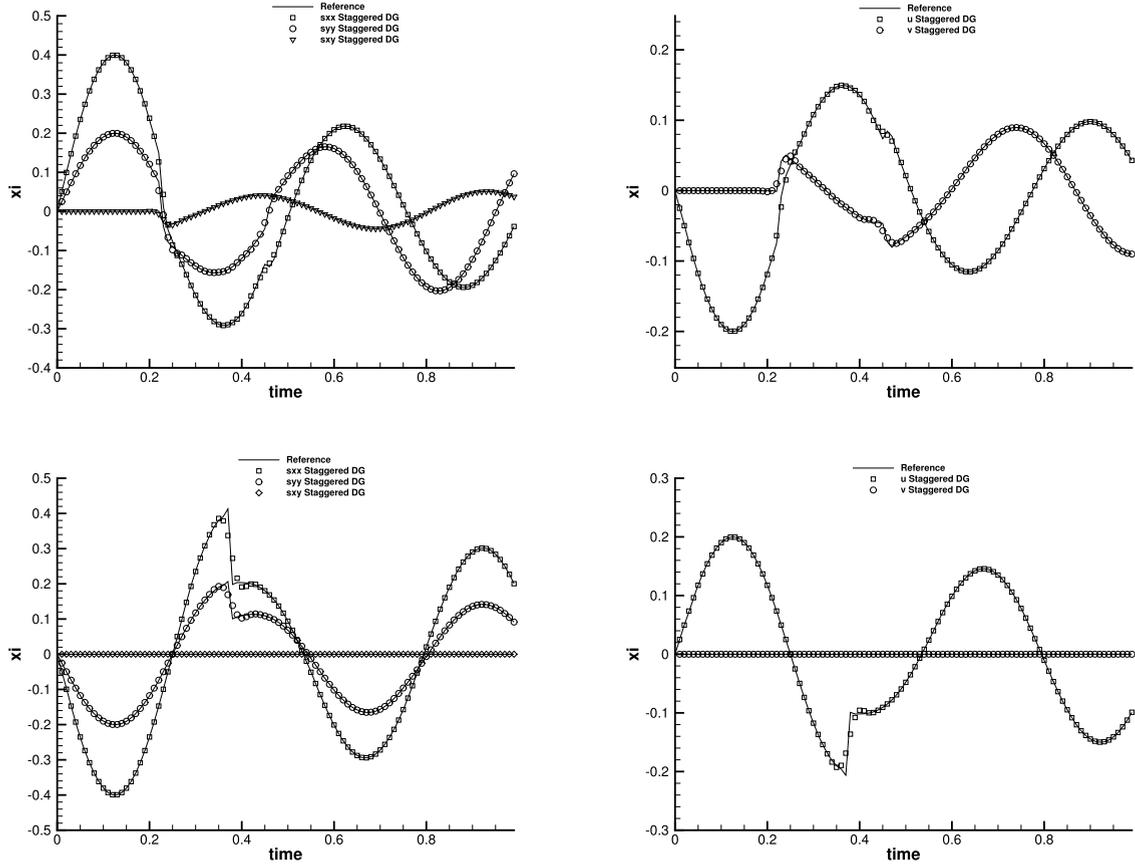**Fig. 4.** Comparison of the stress tensor components σ_{xx}, σ_{yy}, σ_{xy} (left) and velocity components u, v (right) in the receiver point $\mathbf{x}_1 = (0.5, 0.5)$ (top) and $\mathbf{x}_2 = (1.0, 0.0)$ (bottom).

where $\alpha = 0.1$; $\mathbf{k} = 2\pi \, \mathbf{n}$; $\mathbf{n} = (n_x, n_y) = (1, 1)$; $\mathbf{r}_p$ and $\mathbf{r}_s$ are the eigenvectors associated with the p- and s-wave:

$$\mathbf{r}_s = \left(-2\mu n_x n_y, \, 2\mu n_x n_y, \, \mu(n_x^2 - n_y^2), \, n_y c_s, \, -n_x c_s \right), \qquad \mathbf{r}_p = \left(\lambda + 2\mu n_x^2, \, \lambda + 2\mu n_y^2, \, 2\mu n_x n_y, \, -n_x c_p, \, -n_y c_p \right),$$

(59)

with the p-wave speed $c_p = \sqrt{(\lambda + 2\mu)/\rho}$ and the s-wave speed $c_s = \sqrt{\mu/\rho}$. We set $(\lambda, \mu, \rho) = (2, 1, 1)$. The final time is $t_{end} = 3\sqrt{2}$ so that the resulting exact solution has to be the same as the initial one i.e. $\mathbf{U}(\mathbf{x}, t_{end}) = \mathbf{U}(\mathbf{x}, 0)$. In Table 1 we report the resulting L_2 error norms for the entire state vector $\mathbf{U}$ and the order of convergence for different polynomial approximation degrees $p = p_\gamma$ on a sequence of successively refined meshes of characteristic size $h = (0.1264, 0.0842, 0.0842, 0.0505, 0.0421)$. The time step size has been chosen proportional to the mesh spacing h as $\Delta t = Kh$, with $K = 0.112$, independent of the polynomial degree p. We also report the wall clock times T_{CPU} measured on 20 cores of an Intel Xeon E5 CPU with 2.5 GHz clock speed and 128 GB of RAM. From Table 1 the optimal order of convergence can be observed for all variables.

6.3. 2D tilted Lamb problem

In this test case we study the two dimensional tilted Lamb problem, as suggested in [15,27]. The computational domain $\Omega = \{(x, y) \in \mathbb{R}^+ \, | \, 0 \leq x \leq 4000 \, , \, 0 \leq y \leq 2000 + x \tan\theta\}$ consists in a free surface with a tilt angle of $\theta = 10°$. The chosen p- and s-wave velocities are set to $c_p = 3200$ and $c_s = 1847.5$, respectively. The mass density is taken as $\rho = 2200$ so that the resulting Lamé constants are $\lambda = 7.5096725 \cdot 10^9$ and $\mu = 7.50916375 \cdot 10^9$. The initial condition is $\mathbf{U} = 0$ everywhere in Ω. The waves are generated by a directional point source located in $\mathbf{x}_s = (1720.0, 2303.18)$. We place a receiver in $\mathbf{x}_p = (2694.96, 2475.08)$, at a distance of 900 length units from the source. As reference solution we use the well established ADER-DG method proposed in [27,28,88] with $N = M = 4$ and $N_i = 844560$. The numerical parameters of the new staggered space–time DG scheme are $p = 4$, $p_\gamma = 2$, $\Delta t = 10^{-3}$ and $N_i = 33952$. The point source

$$\mathbf{S}_v(\mathbf{x}, t) = \frac{1}{\rho} \mathbf{d} \, \delta(\mathbf{x} - \mathbf{x}_s) \mathcal{S}(t),$$

Table 1

Numerical convergence test: L_2 error norm, numerical convergence rates and CPU time T_{CPU} for all variables for $p = p_\gamma = 1 \ldots 4$.

p	N_i	u		v		σ_{xx}		σ_{yy}		σ_{xy}		T_{CPU}
1	1760	1.253E-01		2.675E-01		5.111E-01		3.003E-01		1.343E-01		4.4
1	3960	4.609E-02	2.5	1.284E-01	1.8	2.428E-01	1.8	1.248E-01	2.2	6.143E-02	1.9	11.7
1	7040	2.479E-02	2.2	7.356E-02	1.9	1.387E-01	1.9	6.938E-02	2.0	3.481E-02	2.0	24.3
1	11000	1.567E-02	2.1	4.741E-02	2.0	8.931E-02	2.0	4.430E-02	2.0	2.235E-02	2.0	42.7
p	N_i	u		v		σ_{xx}		σ_{yy}		σ_{xy}		T_{CPU}
2	1760	1.512E-03		3.249E-03		6.081E-03		3.156E-03		1.574E-03		27.6
2	3960	3.697E-04	3.5	6.568E-04	3.9	1.218E-03	4.0	6.411E-04	3.9	3.186E-04	3.9	90.1
2	7040	1.416E-04	3.3	2.118E-04	3.9	3.882E-04	4.0	2.086E-04	3.9	1.031E-04	3.9	198.1
2	11000	6.901E-05	3.2	8.872E-05	3.9	1.601E-04	4.0	8.835E-05	3.9	4.324E-05	3.9	364.4
p	N_i	u		v		σ_{xx}		σ_{yy}		σ_{xy}		T_{CPU}
3	1760	5.522E-05		3.323E-05		4.781E-05		3.835E-05		1.919E-05		153.3
3	3960	1.079E-05	4.0	5.544E-06	4.4	6.534E-06	4.9	6.313E-06	4.4	3.250E-06	4.4	450.5
3	7040	3.414E-06	4.0	1.677E-06	4.2	1.824E-06	4.4	1.906E-06	4.2	9.790E-07	4.2	998.0
3	11000	1.396E-06	4.0	6.827E-07	4.0	7.183E-07	4.2	7.668E-07	4.1	3.983E-07	4.0	1811.5
p	N_i	u		v		σ_{xx}		σ_{yy}		σ_{xy}		T_{CPU}
4	1760	2.480E-06		1.216E-06		1.400E-06		1.434E-06		6.596E-07		183.0
4	3960	3.270E-07	5.0	1.582E-07	5.0	1.820E-07	5.0	1.869E-07	5.0	8.319E-08	5.1	984.6
4	7040	7.724E-08	5.0	3.733E-08	5.0	4.292E-08	5.0	4.418E-08	5.0	1.933E-08	5.1	2476.2
4	11000	2.532E-08	5.0	1.218E-08	5.0	1.402E-08	5.0	1.442E-08	5.0	6.278E-09	5.0	9466.8
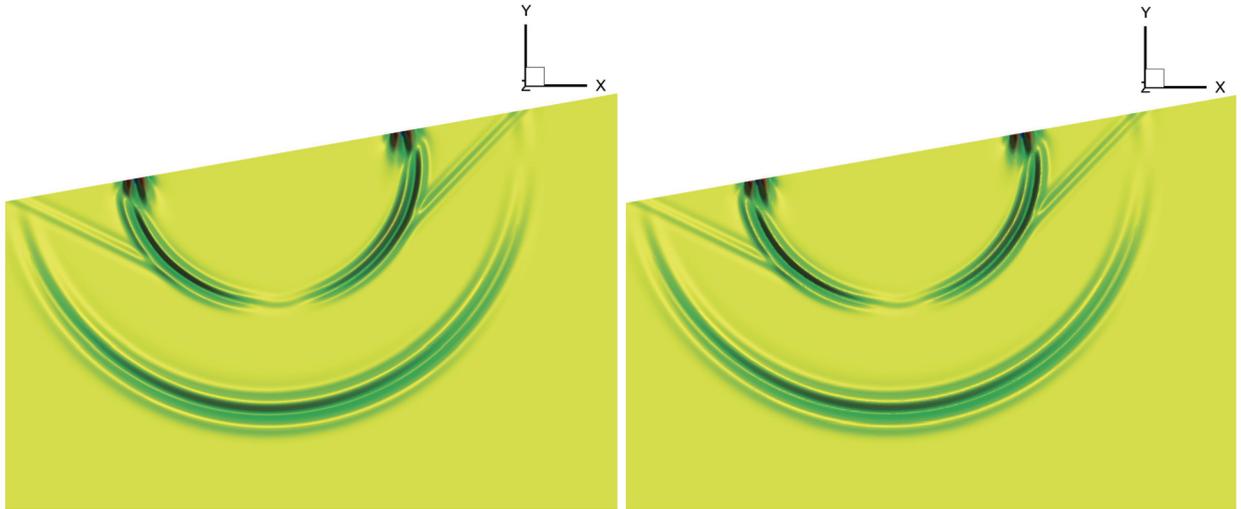
Fig. 5. Contours of the velocity component v at time $t = 0.6$ obtained with an explicit ADER-DG scheme (left) as reference and the new staggered space–time DG scheme (right).

is characterized by a Dirac delta distribution in space located in $\mathbf{x}_s$ and a temporal part, which is a Ricker wavelet defined as

$$S(t) = a_1 \left(0.5 + a_2 (t - t_D)^2 \right), \tag{60}$$

where $t_D = 0.08s$ is the source delay time; $a_1 = -2000$; $a_2 = -(\pi f_c)^2$; and $f_c = 14.5$. Finally the vector $\mathbf{d} = (-\sin\theta, \cos\theta, 0, 0, 0)^\top$ determines the direction of the source and depends on the tilt angle θ. A comparison of the velocity component v at $t = 0.6$ is reported in Fig. 5. Fig. 6 shows the comparison of the recorded seismograms in the receiver location $\mathbf{x}_p$. An excellent agreement with the reference solution can be observed also in this case.

6.4. Wave propagation in complex geometry

This test case is very similar to the previous tilted Lamb problem, but in a non-trivial domain and using a heterogeneous medium. The computational domain is $\Omega = \{(x, y) \mid x \in [0, 4000] \; y \in [0, f(x)]\}$ where the location of the free surface boundary is defined by the function $f(x) = 2000 + 100 \left(\sin\left(\frac{3}{200}x\right) + \sin\left(\frac{2}{200}x\right) \right)$. The material is heterogeneous and consists in two layers with different material properties. The first layer is placed in $\{y > 1500 - \frac{x}{2}\}$ with $c_p = 3200$ and $c_s = 1847.5$,
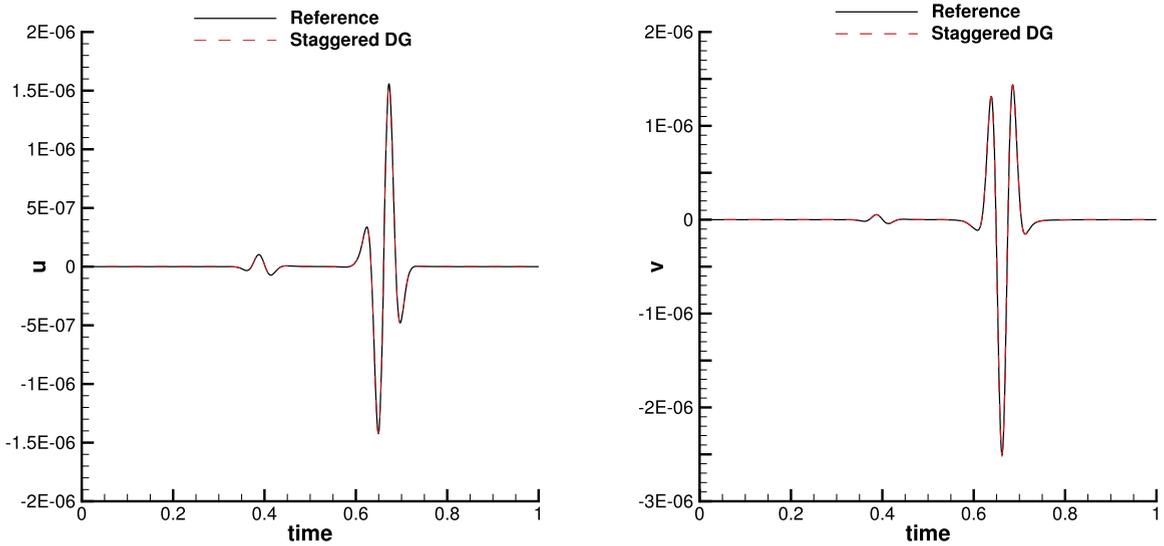
Fig. 6. Comparison of the numerical solution obtained with the new staggered space–time DG scheme and the reference solution for the velocity components u and v in the receiver point $\mathbf{x} = \mathbf{x}_p$ up to $t = 1.0$.
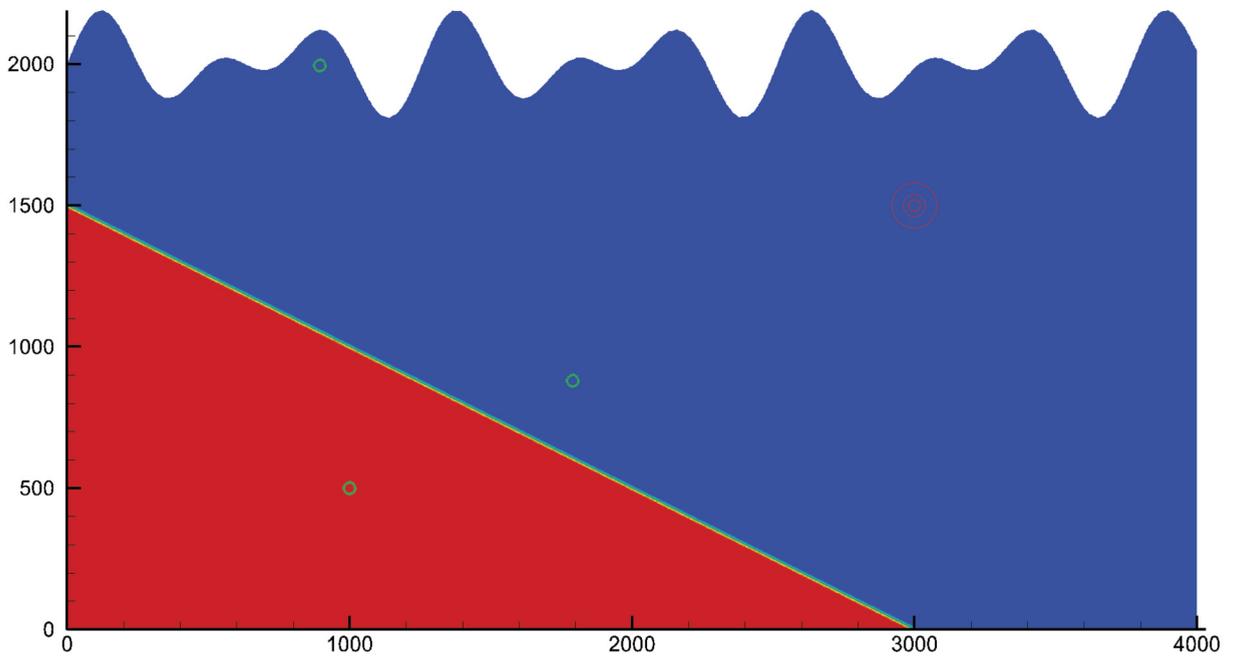

Fig. 7. Wave propagation in complex geometry. Computational domain with the point source highlighted in red and the receivers in green.

while the second layer covers the rest of the domain with $c_p = 2262.74$ and $c_s = 1306.38$. We use free surface boundary conditions everywhere. The same point source as described in the previous Section 6.3 is used (with $\theta = 10°$ as before) and is located in $\mathbf{x}_s = (3000, 1500.18)$. We place three seismogram recorders in $\mathbf{x}_1 = (893.80, 1994.83)$, $\mathbf{x}_2 = (1790.0, 880.0)$ and $\mathbf{x}_3 = (1000.0, 500.0)$. The computational domain, the position of the source point and the position of the receivers are depicted in Fig. 7. The computational domain is discretized using only $N_i = 7352$ triangles of characteristic mesh spacing $h = 58.50$ and the polynomial approximation degrees are chosen as $p = 4$ in space and $p_\gamma = 2$ in time. We run the simulation up to $t = 5$ and we set $\Delta t = 10^{-3}$. We compare our numerical solution again with the well established ADER-DG method proposed in [27,28,88] with $N = M = 4$ on the same spatial mesh. A comparison of the numerical solution with the reference solution is reported at several times in Fig. 8, while the time series of the velocity component v in the three receiver points is reported in Fig. 9. In all cases we can observe a very good agreement with the reference solution.
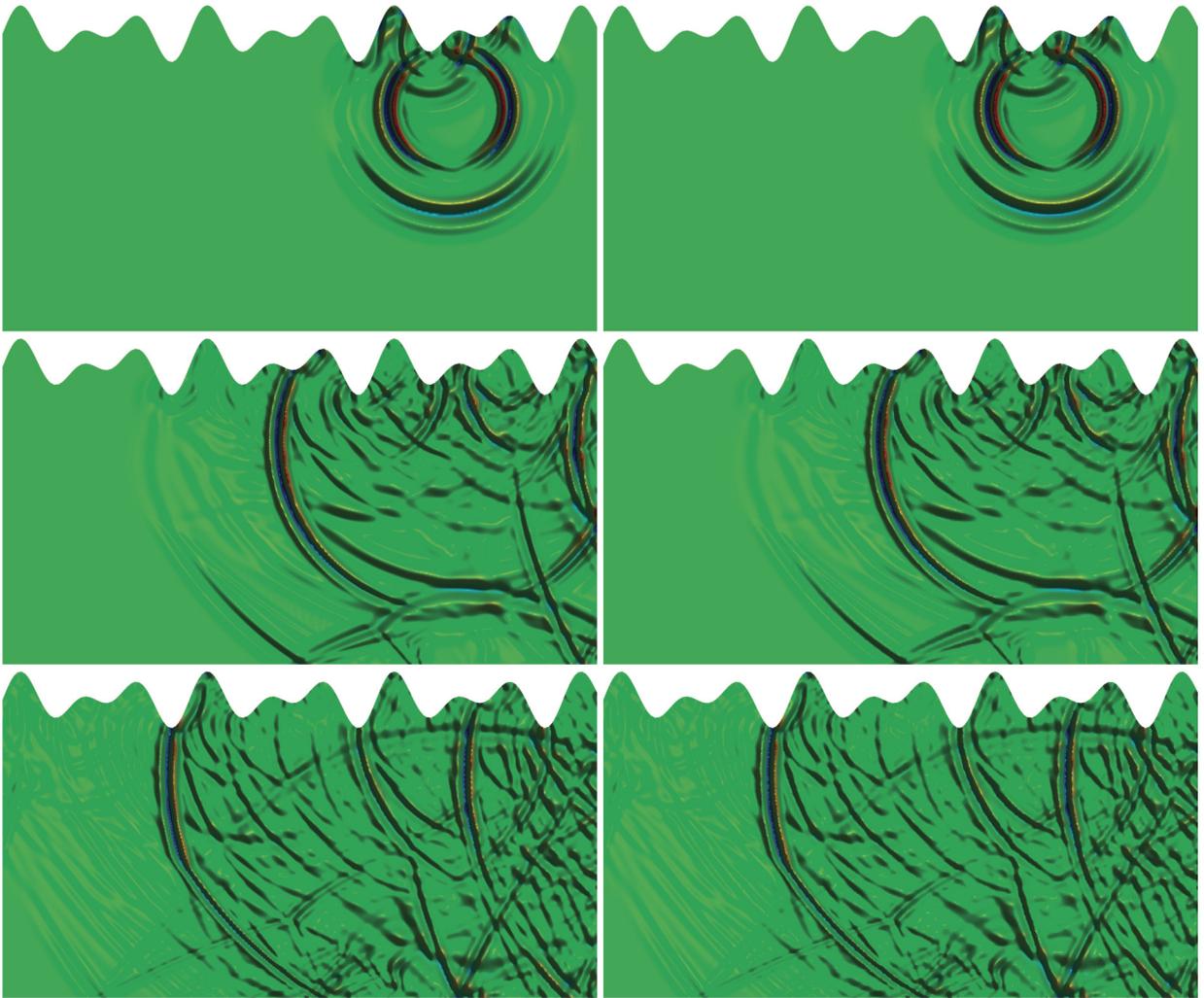
Fig. 8. Wave propagation in complex geometry. Isocontours of the vertical velocity v at times $t = 0.3, 0.7, 1.1$ from top to bottom for the reference solution (left) and the new staggered space–time DG scheme (right).

6.5. Sliver element problem

Since in unstructured meshes for complex geometries or Cartesian cut cell approaches one can easily generate so-called *sliver elements*, we want to test our new approach in the case where we have sliver elements in the computational domain, see [31] for a similar study in the context of explicit ADER-DG schemes with time-accurate local time stepping (LTS). We will compare the number of iterations needed to solve the linear system in the case of a regular unstructured grid and the mesh containing the sliver elements. Since the resulting matrix for the velocity field becomes locally ill-conditioned, we will use here a couple of preconditioners in order to control the number of iterations. The simplest one (Pre1) consists in inverting only the diagonal block of the system matrix, while the second one (Pre2) requires to invert a local system composed of the element and its direct face neighbors. More details about the construction of those preconditioners are reported in Appendix A. We consider a computational domain $\Omega = [-1.5, 1.5]^2$ covered with an almost uniform grid (mesh 1) and the same grid with two strongly deformed sliver elements (mesh 2), see Fig. 10. The incircle radius corresponding to the sliver elements in mesh 2 is reduced by a factor of 70.53 with respect to mesh 1. We use the same setup as presented in Section 6.2 for a simple p-wave traveling in direction $\mathbf{n} = (1, 0)$ and we use $(p, p_\gamma) = (4, 2)$ with a time step size of $\Delta t = 0.014$ for both meshes. This is possible since our staggered space–time DG scheme is *unconditionally stable*. Fig. 11 shows the numerical solutions obtained on the two different meshes. One can observe that the introduction of the sliver element in mesh 2 does not change the quality of the solution, but of course it changes the effort required to solve the linear system for the velocity. The mean number of iterations needed to solve the system is reported in Table 2. The trend of the iterations in the different cases is shown in Fig. 12. As we can easily see, if we do not use any kind of preconditioner, the average number of iterations increases a lot. The use of the fully local preconditioner 1 helps to reduce the number of
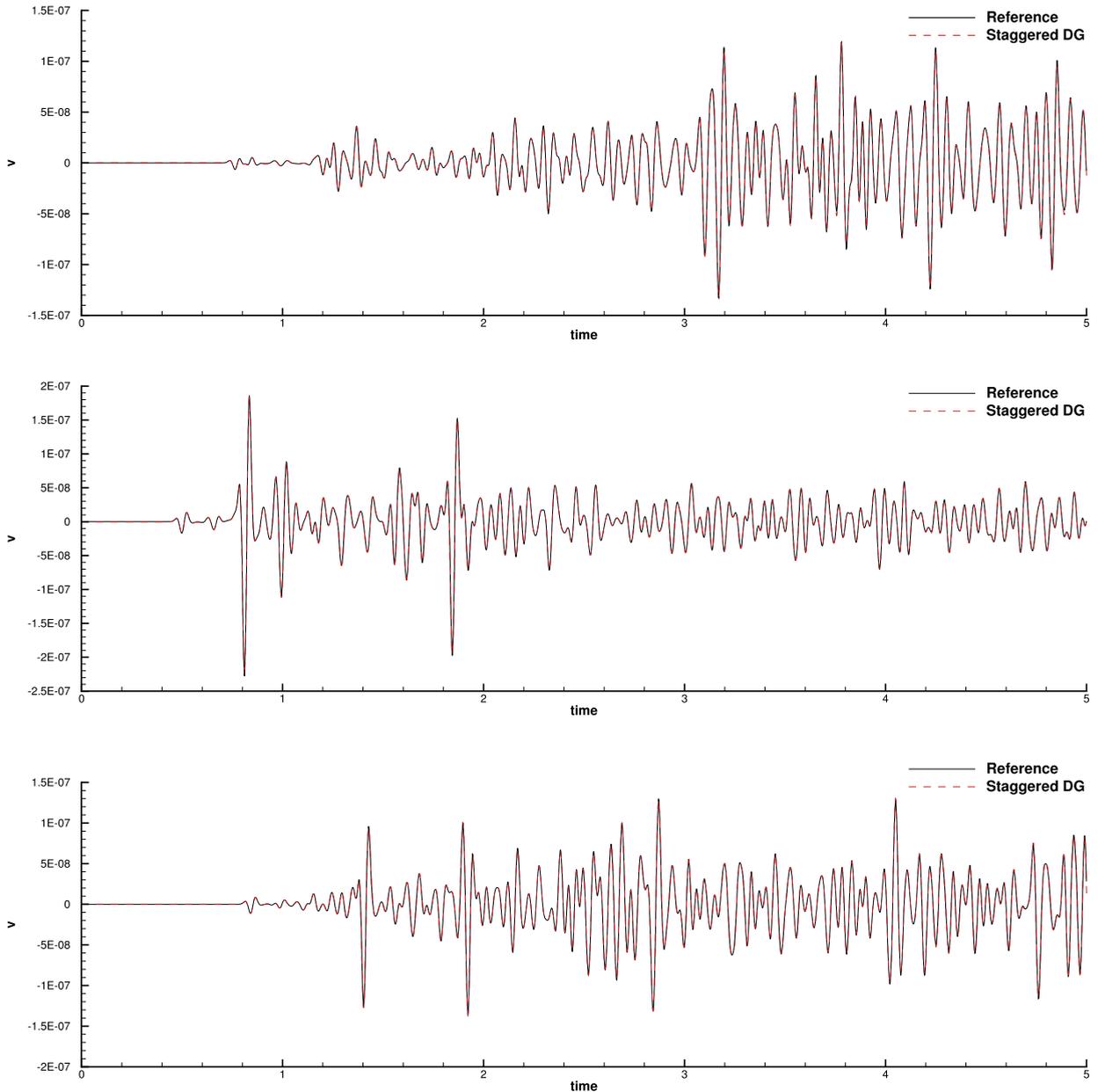
Fig. 9. Comparison between numerical and reference time series for the velocity component v in the three receivers $1 \ldots 3$ from top to bottom.

iterations, while the second preconditioner is sufficient to solve this ill-conditioning problem and to keep the number of iterations almost independent of the mesh.

6.6. 3D wave propagation

In this test case we want to check our numerical method in three space dimensions. We take a very simple material block of size $\Omega = [0, 10000] \times [-8000, 2000] \times [-5000, 5000]$. We use a homogeneous material with $c_p = 3200$, $c_s = 1847.5$ and $\rho = 2200$. The resulting Lamé constants are $\lambda = 7.51 \cdot 10^9$ and $\mu = 7.51 \cdot 10^9$. The domain is covered with $N_i = 214893$ tetrahedral elements of average size $h = 388.55$. For this test problem we use the particular case of the Crank–Nicolson time discretization ($p_\gamma = 0$) and approximation degree $p = 4$ in space. The wave is generated by an initial Gaussian profile imposed in the velocity component w as

$$w(\mathbf{x}, 0) = a e^{-r^2/R^2} \tag{61}$$
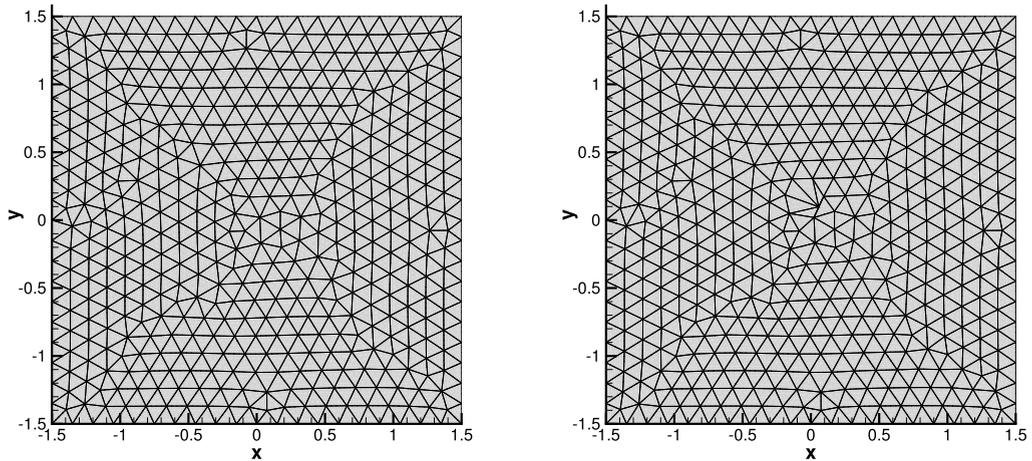
Fig. 10. Almost uniform mesh 1 (left) and mesh 2 containing two sliver elements (right).
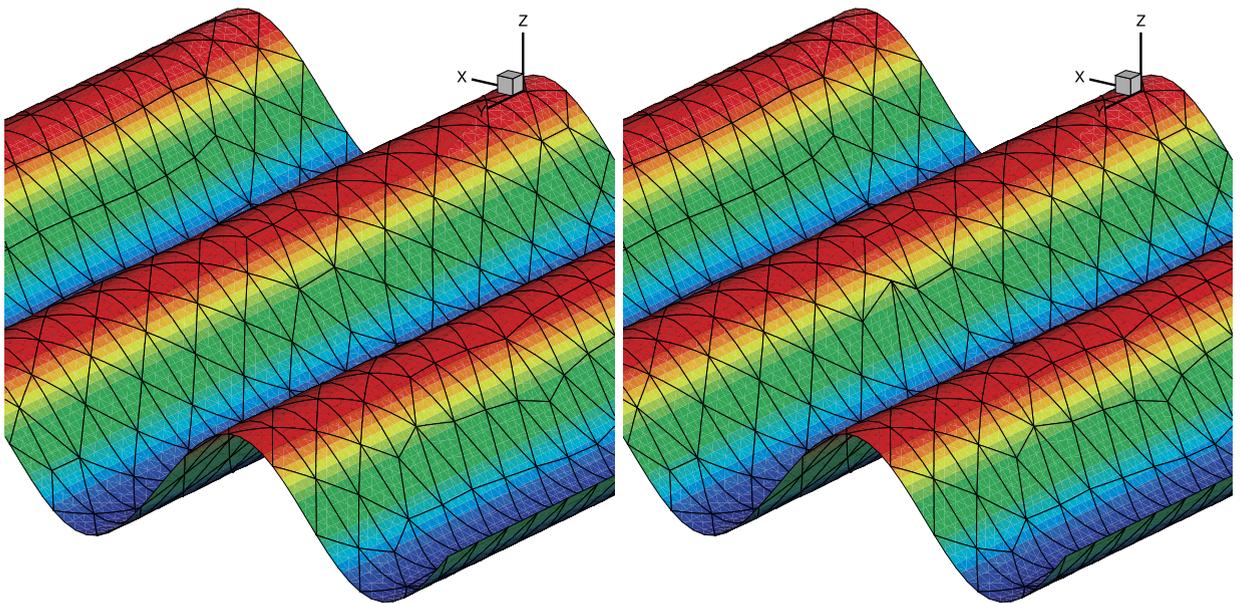
Fig. 11. Numerical results for the velocity component u using the regular unstructured mesh 1 (left) and the unstructured mesh 2 containing the sliver elements (right). It can be clearly noted that also on mesh 2 the solution is smooth and is not affected by the presence of the slivers.

Table 2
Number of average iterations needed for the GMRES algorithm with different preconditioners on the uniform unstructured grid (mesh 1) and the one containing the sliver elements (mesh 2).

Preconditioning	Iter. mesh 1	Iter. mesh 2	Factor
None	112.59	611.95	5.43
Pre 1	86.73	191.77	2.21
Pre 2	53.27	53.38	1.00

with $a = -10^{-2}$, $R = 100$ and $r = |\mathbf{x} - \mathbf{x}_0|$ is the distance from the center point $\mathbf{x}_0 = (5000, 1900, 0)$. All other state variables are initialized with zero. We place two receivers in Ω, one close to the free surface at $\mathbf{x}_1 = (6000, 1999, 500)$ and the second one 500 units below the free surface in $\mathbf{x}_2 = (6000, 1500, 500)$. A comparison of the velocity component v obtained with the ADER-DG reference code SeisSol and the new staggered DG scheme proposed in this paper is shown in Fig. 13, where we also show the location of the two receivers. For the computation of the reference solution, we use the same
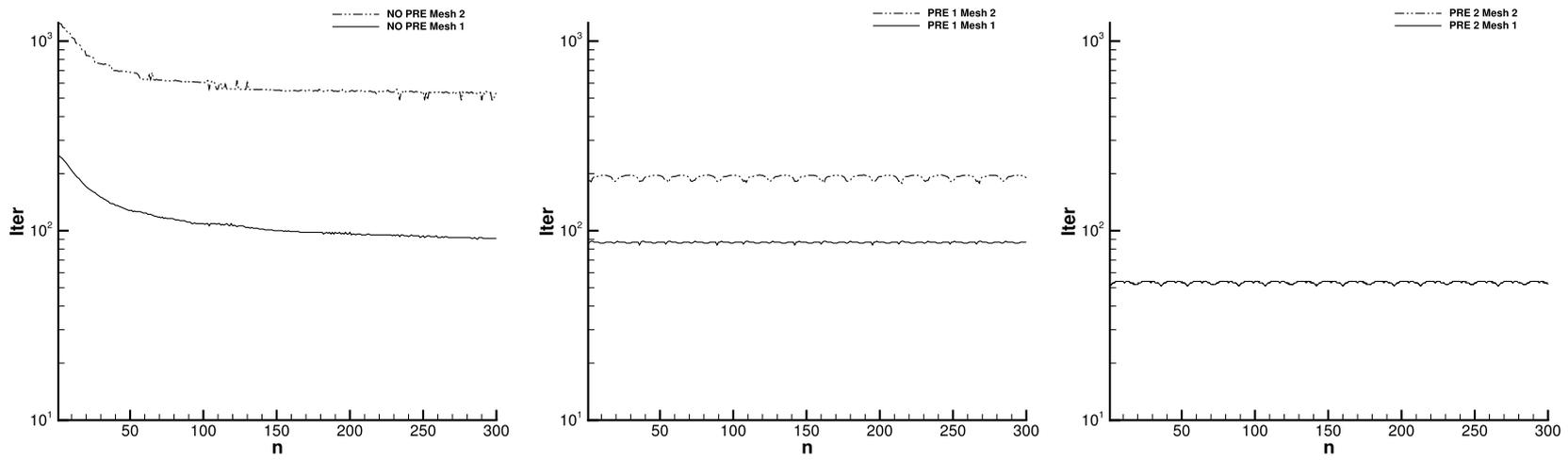
Fig. 12. Required number of iterations for the solution of the linear system plotted over the time step index n in the case of no preconditioning (left), using the preconditioner 1 (center) and the preconditioner 2 (right).
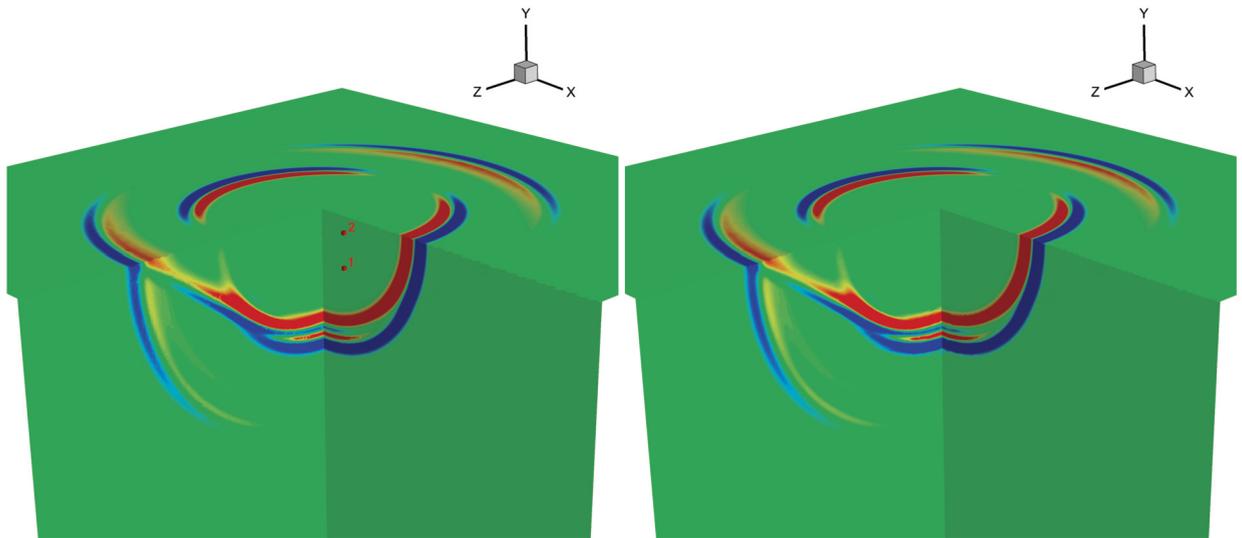
Fig. 13. Simple 3D wave propagation problem. Numerical solution obtained for the velocity component w at time $t = 1.0$ using an explicit ADER-DG reference scheme (left) and the new implicit staggered DG approach presented in this paper (right).

computational mesh and the same order of accuracy, i.e. we use $N = M = 4$ and $N_i = 214893$. In Figs. 14 and 15 we present a comparison between of the time signal recorded in the two receivers with the two different schemes. We can observe a very good agreement between the ADER-DG reference solution and the numerical solution obtained with the new staggered DG scheme. We can also observe that the stress components corresponding to the y direction vanish at the free surface, as reported in Fig. 15.

6.7. Scattering of a planar wave on a sphere

We consider here the 3D extension of the test reported in Section 6.1, which consists of a planar p-wave traveling in the x-direction and hitting a sphere. The computational domain is $\Omega = [-3, 3]^3 - B_{0.25}$, where B_r is the ball of radius r. As numerical parameters we set $N_i = 31732$ elements of average size $h = 0.42$, $(p, p_\gamma) = (4, 2)$, $\Delta t = 0.01$ and $t_{end} = 1.0s$. We consider three receivers placed in $\mathbf{x}_1 = (-1, 0, 0)$, $\mathbf{x}_2 = (0, -1, 0)$ and $\mathbf{x}_3 = (0.5, 0.5, 0.5)$. As a reference solution we use again the explicit ADER-DG scheme implemented in the `SeisSol` code using the same grid and piecewise polynomials of degree $N = 4$ in space and time. The time series in the three receivers are reported in Fig. 16. A very good agreement between the explicit ADER-DG scheme and the novel staggered space–time DG method can be observed also in this case.

6.8. Wave propagation in a complex 3D geometry

We finally want to test the potential of our new numerical scheme for real applications. For this purpose we generate a tetrahedral mesh based on the real DTM data of the Mont Blanc region.[1] The horizontal extent of the domain is 30 km in the x and y directions and ranges from 10 km below the sea level to the free surface given by the DTM data. We use a heterogeneous material distribution consisting in two different material layers. The first one is in the region $\{z > -1000\}$ m, while the second one covers the region $z \leq -1000$ m. The parameters for the material are reported in Table 3. An initial velocity perturbation is placed in $\mathbf{x} = (0, 0, 0)$ for the vertical component of the velocity

$$w(\mathbf{x}, 0) = a e^{-r^2/R^2}, \tag{62}$$

with $a = -10^{-2}$ and $R = 300$ m. All other variables are set to zero. The computational domain is covered with $N_i = 288998$ tetrahedra, whose characteristic size is 500 m close to the free surface and 3000 m far from it. For this test we use $p = 4$ and the Crank–Nicolson time discretization, for which we have the discrete energy preserving property. Furthermore, we set $\Delta t = 10^{-3}$ s and $t_{end} = 4.0$ s. As reference solution we use again the explicit ADER-DG scheme used in the `SeisSol` code with the same mesh and a polynomial approximation degree in space and time of $N = 4$. A comparison of the numerical solution obtained with the new implicit staggered DG scheme and the explicit ADER-DG method at $t = 4.0$ is shown in

---

[1] The DTM data have been taken from http://geodati.fmach.it/gfoss_geodata/libro_gfoss/. Our computational domain is centered with respect to the UTM coordinates (340000.0, 5075000.0).
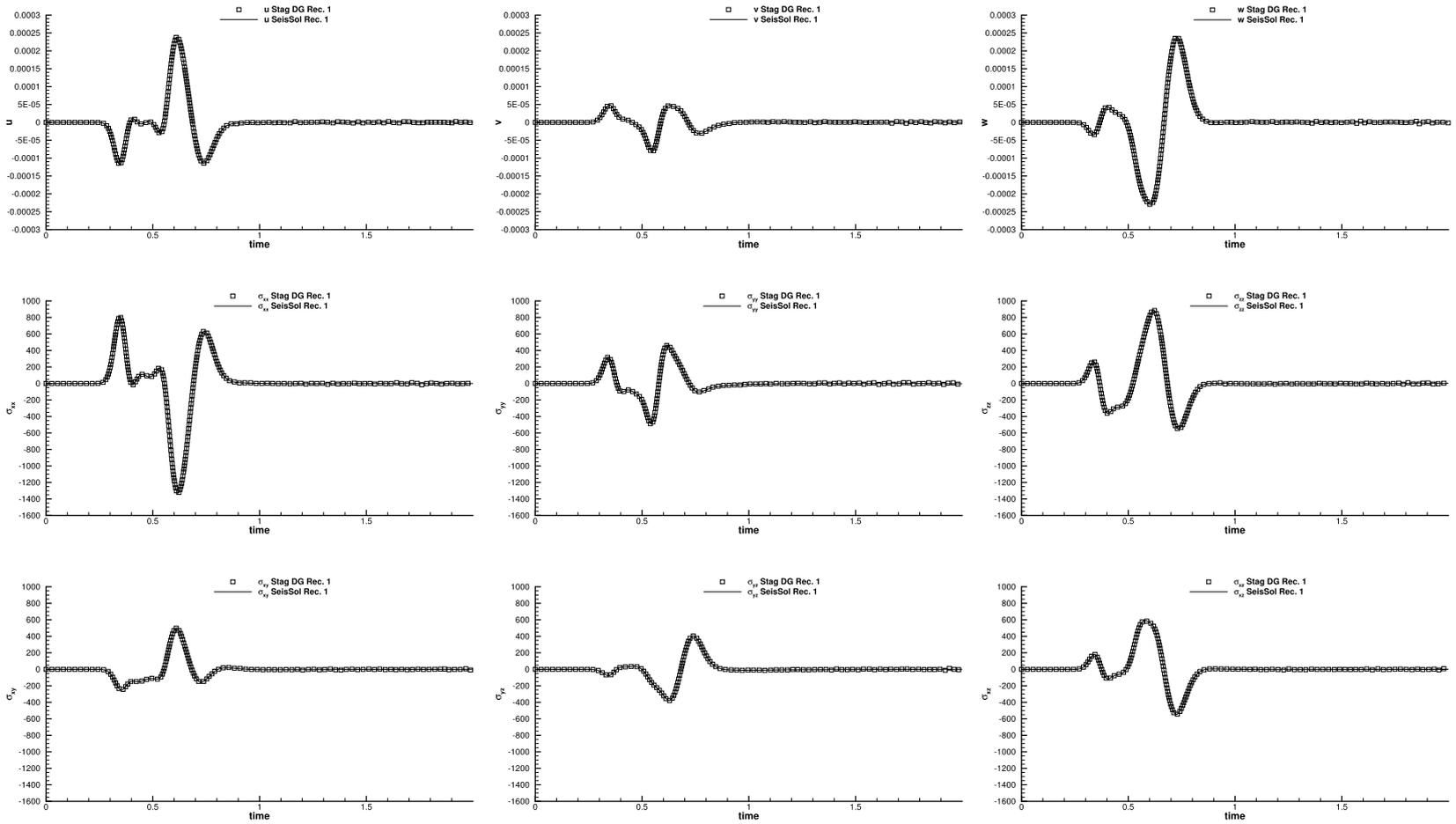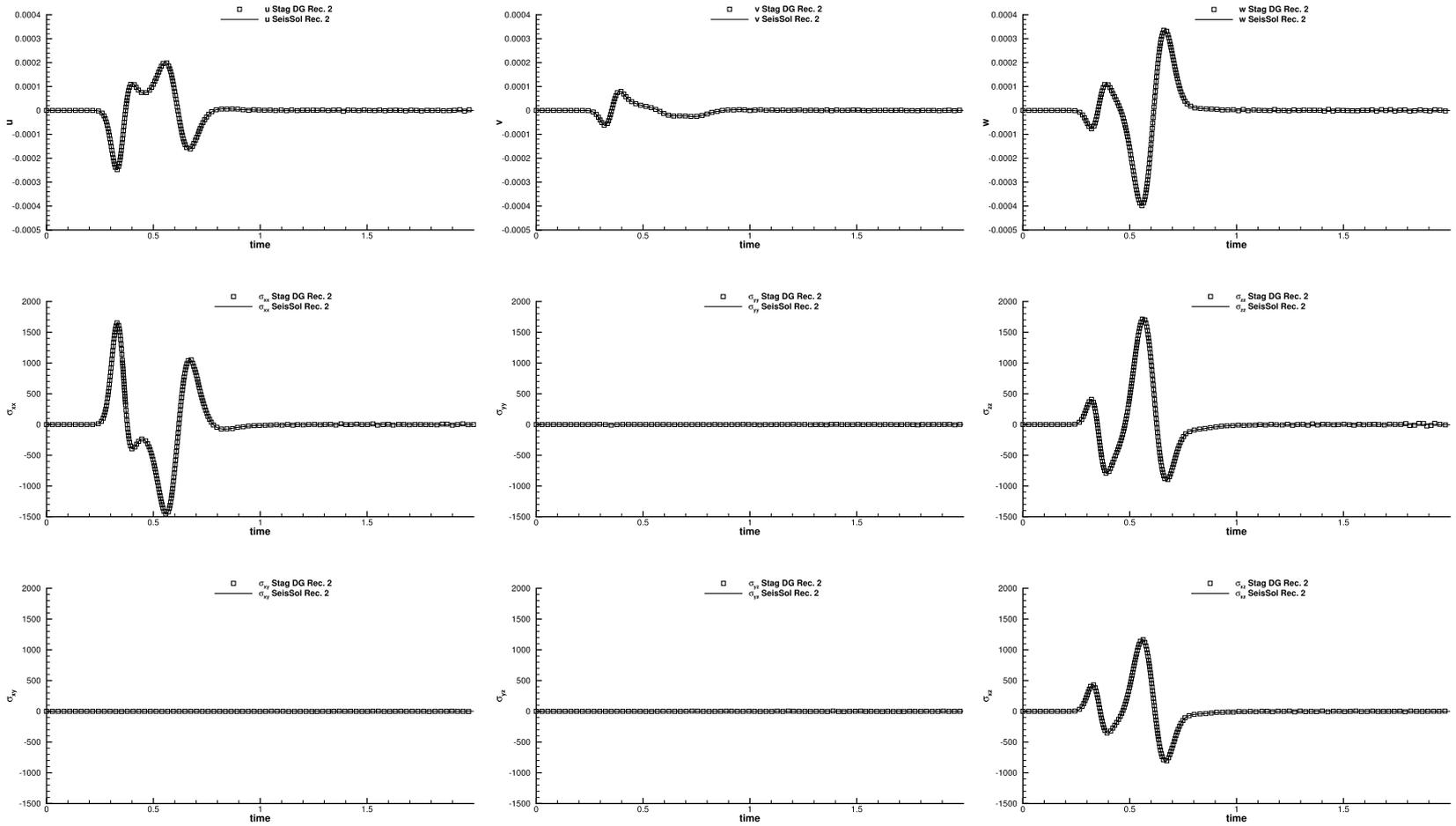
Fig. 14. Simple 3D wave propagation problem. Comparison of the numerical and reference solution in the first receiver, from top left to bottom right: $u, v, w, \sigma_{xx}, \sigma_{yy}, \sigma_{zz}, \sigma_{xy}, \sigma_{yz}, \sigma_{xz}$.

Fig. 15. Simple 3D wave propagation problem. Comparison of the numerical and reference solution in the second receiver, from top left to bottom right: u, v, w, σ_{xx}, σ_{yy}, σ_{zz}, σ_{xy}, σ_{yz}, σ_{xz}.
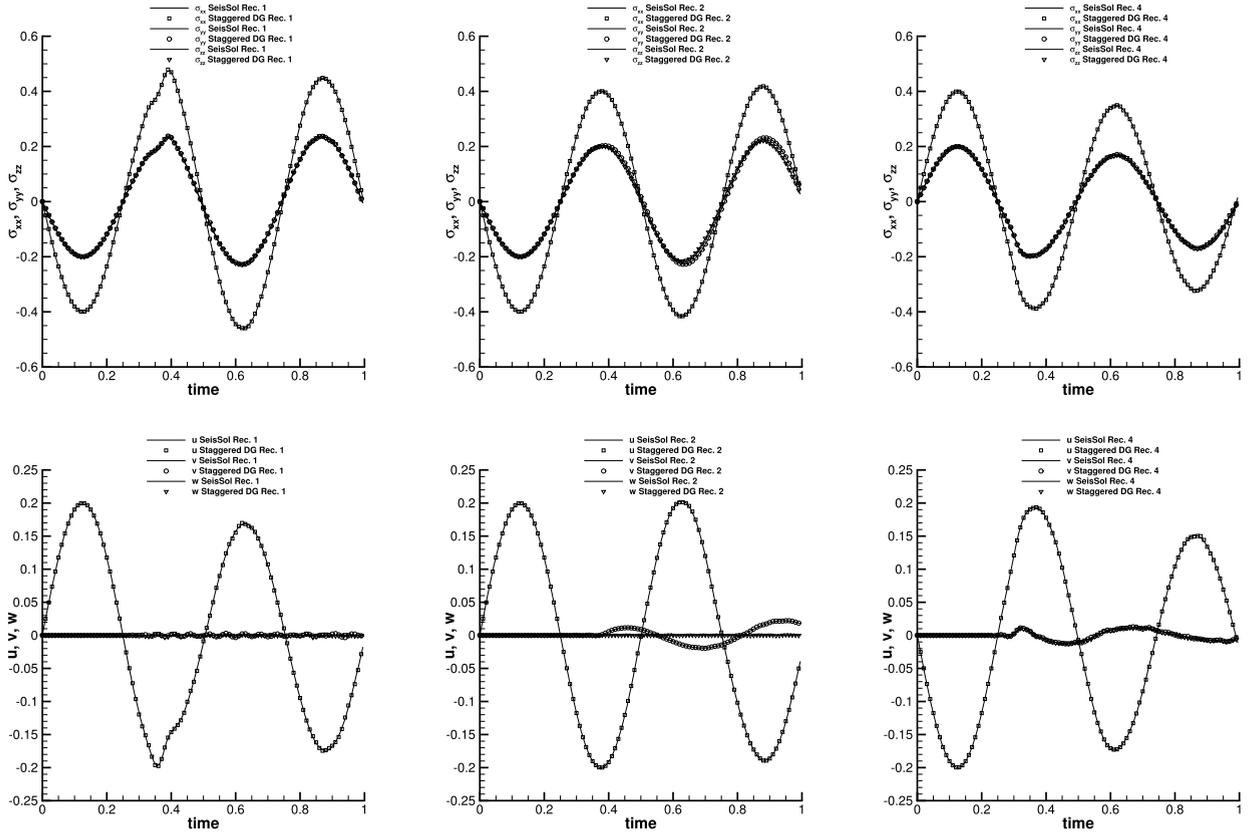
Fig. 16. Scattering of a plane wave on a sphere. Comparison of the resulting signal in the three receivers. In the first row we report the time series of the stress tensor components σ_{xx}, σ_{yy} and σ_{zz} for the receivers 1, 2, 3, respectively, from left to right. In the second row the velocity signal is reported for the same receivers.

Table 3
Material parameters for the wave propagation test in a complex 3D geometry.

	Position	c_p (m s^{-1})	c_s (m s^{-1})	ρ (kg m^{-3})	λ (GPa)	μ (GPa)
Medium 1	$z > -1000$ m	4000	2000	2600	20.8	10.4
Medium 2	$z \leq -1000$ m	6000	3464	2700	32.4	32.4

Fig. 17. We consider also the signal captured in four receivers, whose positions are reported in Table 4 and which are also graphically represented in the right panel of Fig. 17. The resulting time history of the velocity signals for the four receivers is reported in Fig. 18. A very good agreement between the new staggered DG scheme and the reference scheme can be observed also in this case with complex 3D geometry. It is important to note that the use of the energy preserving variant is crucial here to obtain the proper wave amplitude with the new staggered implicit DG method. Furthermore, we can use the simple matrix-free conjugate gradient method in this case, thanks to the good properties of the matrix for the discrete wave equation for the velocity (26), which is symmetric and positive definite for $p_\gamma = 0$. The computation was performed in parallel on the HazelHen supercomputer at the HLRS in Stuttgart, Germany, using 144 Xeon E5-2680 Cores. The parallelization of both schemes was achieved by using the pure MPI standard. It has to be stressed that the MPI parallelization of our new staggered space–time DG scheme is straightforward, since we use a matrix-free iterative Krylov subspace method for the solution of the linear system (26), and the parallelization of the matrix-vector product inside the iterative solver can be done exactly in the same way as for an explicit ADER-DG scheme, i.e. based on domain decomposition. As in [28,31] we employ the free Metis software package [89] for the domain decomposition onto the various MPI ranks.

7. Conclusions

In this paper we have introduced a novel family of staggered space–time discontinuous Galerkin finite element schemes for the simulation of wave propagation in linear elastic media. The governing PDE system is written in first order velocity-stress formulation. The key idea is the use of a staggered mesh, where the velocity field is defined on a primary mesh composed of simplex elements, i.e. triangles in 2D and tetrahedra in 3D. The stress tensor is defined on a face-based stag-
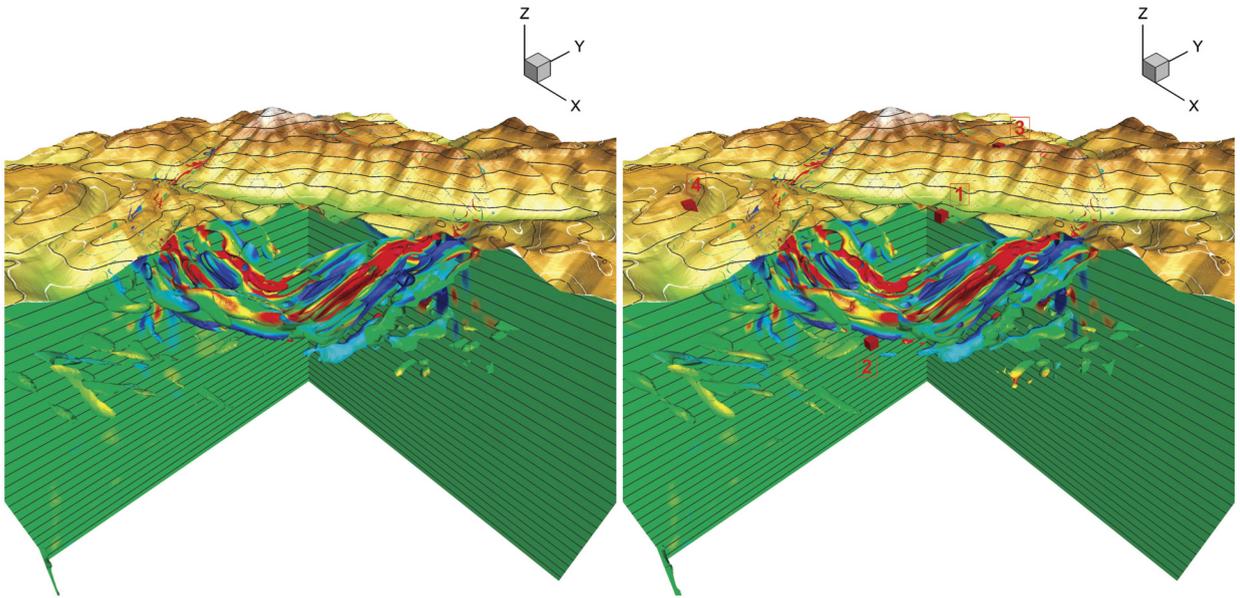
Fig. 17. Wave propagation test in a complex 3D geometry with real DTM data of the Mont Blanc region. Comparison of the explicit ADER-DG reference solution (left) with the numerical solution obtained with the new implicit staggered DG scheme (right) at time $t = 4.0$. In the right panel the receiver locations are indicated by the red boxes. We show the iso-surfaces $\pm 5 \cdot 10^{-5}$ for the velocity components u and v colored by w.

Table 4
Receiver positions for the wave propagation test in complex 3D geometry.

Receiver	x	y	z
1	1000.000000	0.000000	1397.723250
2	1545.084972	−4755.282581	−3000.000000
3	0.000000	5000.000000	3231.607925
4	−5000.000000	−8660.254038	2494.481430

gered dual mesh, which consists in quadrilateral elements in the 2D case and non-standard 5-point hexahedra in the 3D case. Arbitrary high order of accuracy in space and time are achieved via the use of space–time basis and test functions. The space–time DG method is fully implicit and therefore requires the solution of a large sparse linear system. The number of unknowns can be easily reduced to the degrees of freedom of the velocity field by substituting the discrete Hooke law into the discrete momentum conservation law, which corresponds to the application of the Schur complement. The resulting linear system for the velocity is a discrete wave equation for the velocity and can be easily solved with modern iterative Krylov methods. For piecewise constant polynomials in time ($p_\gamma = 0$) the final system can be proven to be symmetric and positive definite, hence it can be efficiently solved with a matrix-free conjugate gradient method. In the general case ($p_\gamma \geq 1$) the system is non-symmetric and is therefore solved with a matrix-free implementation of the GMRES algorithm. The use of matrix-free iterative solvers allows a straightforward MPI parallelization of the algorithm on modern supercomputers.

The main advantage of our new staggered space–time DG scheme is its unconditional stability and therefore its robustness with respect to the mesh quality. In particular in complex 3D geometries, it is very frequent that computational meshes generated even by modern mesh generation software produce so-called sliver elements, which are elements with a very high aspect ratio. Although our new method is unconditionally stable, for computational meshes that contain sliver elements, the linear system becomes ill-conditioned and therefore requires the use of a preconditioner. We have implemented two simple preconditioners: the first one is element-local and is based on the exact inverse of each block on the diagonal of the system matrix; the second one is more sophisticated and requires the inverse of the local system involving the element and its direct face neighbors. In numerical experiments we have found that the second preconditioner is fully sufficient to deal with sliver elements. For the general case we can prove that the method is energy stable for arbitrary meshes and time step size. For the special case of a Crank–Nicolson time discretization, the method is proven to be exactly energy conserving. We have applied the method to a large set of test problems in two and three space dimensions and we have also studied the convergence of the scheme via numerical experiments on a smooth problem with exact solution. In all cases the new approach produces excellent results. The new numerical method presented in this paper is sufficiently general to allow varying material properties within each element and even anisotropic material behavior could be handled in principle.

Future work will concern the extension of the method to dynamic rupture processes following the ideas outlined in [90,91] for high order ADER-DG schemes. We furthermore plan to couple the present staggered space–time DG scheme with
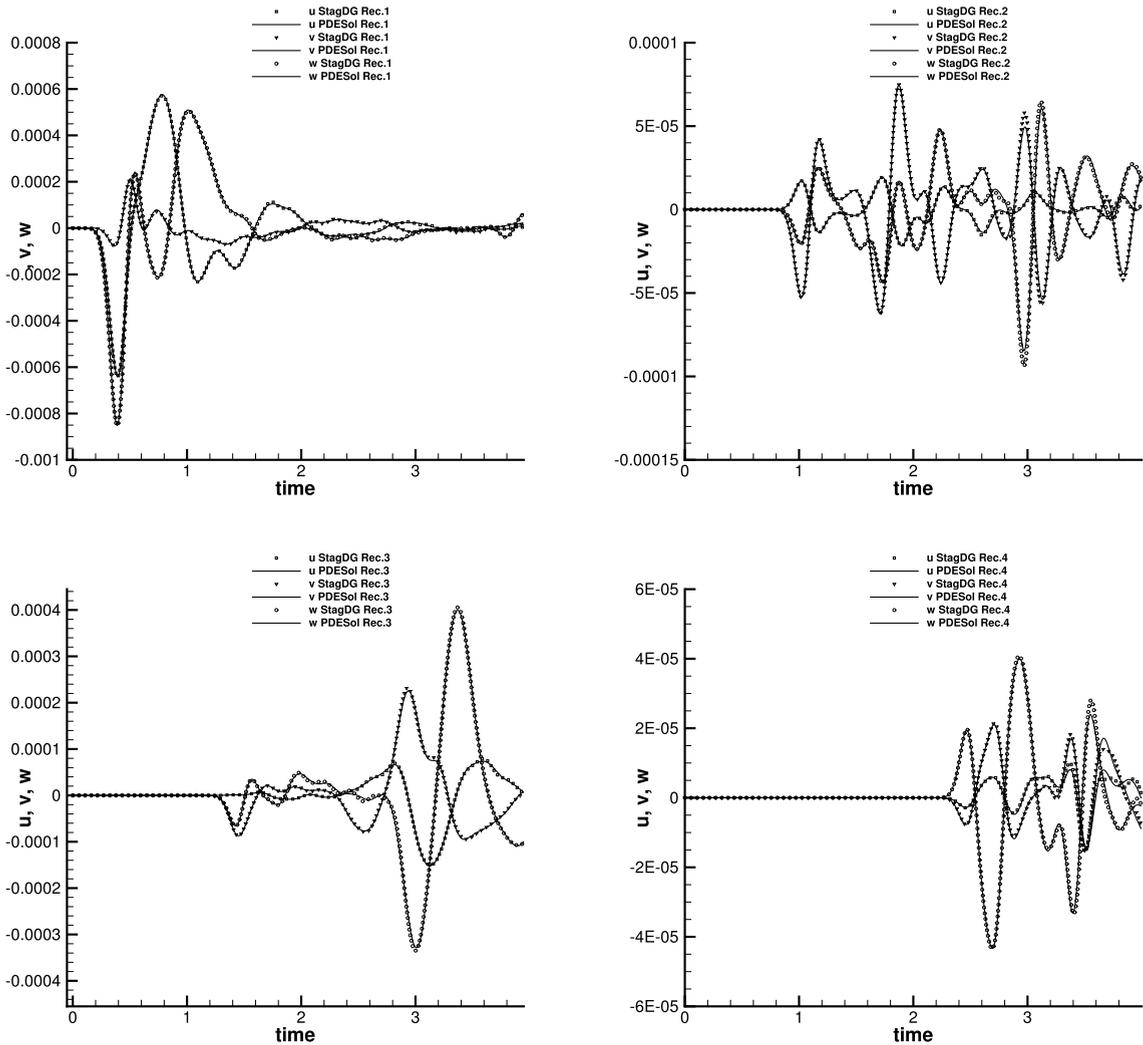
Fig. 18. Wave propagation test in a complex 3D geometry. Comparison of the numerical solution obtained with the new staggered DG scheme presented in this paper with the reference solution for receivers 1–4, respectively, from top left to bottom right.

explicit ADER-DG methods on adaptive Cartesian meshes (AMR), see [92,46]. Further work will also concern the generalization of the present scheme from simple linear elasticity to the equations of fully nonlinear hyperelasticity of Godunov and Romenski [93] and their recent extension to a unified formulation of continuum mechanics achieved by Peshkov and Romenski and collaborators in [94–96]. Last but not least, we plan to extend our scheme to the Maxwell and MHD equations, where staggered meshes are necessary in order to enforce a divergence-free magnetic field. In particular, we plan to couple the present approach with some of the novel ideas recently outlined in [97–100] concerning the use of multi-dimensional Riemann solvers combined with appropriately staggered meshes for the solution of the Maxwell and MHD equations.

Acknowledgements

Appendix A. Preconditioning

Here we give some more details on how to implement the two simple preconditioners used to solve the sliver element test problem. For the first preconditioner, we only take the diagonal block of system (26), which for the high order staggered space–time DG method reads

$$\mathbf{D}_i = \bar{\mathbf{M}}_i \,\hat{\rho}_i - \sum_{j \in S_i} \mathcal{D}_{i,j} \mathbf{M}_j^{-1} \hat{\mathbf{E}}_j \cdot \mathcal{Q}_{i,j}. \tag{A.1}$$

We then exactly invert it for each element and use the block-diagonal matrix $\mathcal{P}_1 = \text{diag}\left(\mathbf{D}_1^{-1}, \cdots \mathbf{D}_i^{-1}, \cdots \mathbf{D}_{N_i}^{-1}\right)$ as preconditioner number one.

The second preconditioner is more sophisticated and locally inverts a small linear system for each element involving also its neighbor elements. Let us locally renumber the elements around T_i^{st} so that $i \to 0$ and the adjacent face neighbors are numbered as $\wp(i, j) = \{1, 2, 3\}$ in 2D and $\wp(i, j) = \{1, 2, 3, 4\}$ in 3D. Let us denote the contributions of the neighbors to the linear system by the off-diagonal blocks $\mathbf{N}_{l,m}$, which represent the contribution of element m on element l. For the second preconditioner we now assemble a local system around T_i^{st} which involves T_i^{st} and its direct face neighbors and which constitute a local stencil S_i. In the following we will denote by $|S_i| = d + 2$ the number of elements contained in the local stencil, where d is the number of space dimensions. Using the renumbering of the elements, the auxiliary system matrix $\mathbf{A}_i$ for the local system reads in 2D

$$\mathbf{A}_i = \begin{pmatrix} \mathbf{D}_0 & \mathbf{N}_{0,1} & \mathbf{N}_{0,2} & \mathbf{N}_{0,3} \\ \mathbf{N}_{1,0} & \mathbf{D}_1 & \mathbf{N}_{1,2} & \mathbf{N}_{1,3} \\ \mathbf{N}_{2,0} & \mathbf{N}_{2,1} & \mathbf{D}_2 & \mathbf{N}_{2,3} \\ \mathbf{N}_{3,0} & \mathbf{N}_{3,1} & \mathbf{N}_{3,2} & \mathbf{D}_3 \end{pmatrix}. \tag{A.2}$$

The matrix $\mathbf{A}_i$ has dimension $N_\phi^{st} \cdot d \cdot |S_i|$, and so it is easily invertible in a preprocessing step using a direct solver. We can therefore compute its inverse $\mathbf{A}_i^{-1}$ for each element and store its first row of blocks. With $\mathbf{A}_i^{-1}(e_1, e_2)$ for $e_1, e_2 = 0 \ldots |S_i| - 1$ we will denote the subblock in the inverse of $\mathbf{A}_i$ which corresponds to the interaction of element e_1 with e_2. The action of the preconditioner matrix $\mathcal{P}_2$ is then given for each element i by

$$\mathcal{P}_2 \hat{\mathbf{v}}_i^{n+1} = \sum_{e=0}^{|S_i|-1} \mathbf{A}_i^{-1}(0, e) \hat{\mathbf{v}}_g^{n+1}, \tag{A.3}$$

where $g = g(e)$ corresponds again to the global element number of the local index e. The computational cost of this preconditioner is $N_\phi^{st} \cdot d \cdot |S_i| \cdot N_i$ and so is of the same order of the matrix-vector product required in the iterative solver.

References

[1] R. Madariaga, Dynamics of an expanding circular fault, Bull. Seismol. Soc. Am. 66 (1976) 639–666.
[2] J. Virieux, Sh-wave propagation in heterogeneous media: velocity-stress finite-difference method, Geophysics 49 (1984) 1933–1942.
[3] J. Virieux, P-sv wave propagation in heterogeneous media: velocity-stress finite-difference method, Geophysics 51 (1984) 889–901.
[4] A. Levander, Fourth-order finite difference p-sv seismograms, Geophysics 53 (1988) 1425–1436.
[5] P. Mora, Modeling anisotropic seismic waves in 3-d, SEG Soc. Explor. Geophys. (1989) 1039–1043.
[6] P. Moczo, J. Kristek, V. Vavrycuk, R. Archuleta, L. Halada, 3D heterogeneous staggered-grid finite-difference modeling of seismic motion with volume harmonic and arithmetic averaging of elastic moduli and densities, Bull. Seismol. Soc. Am. 92 (2002) 3042–3066.
[7] H. Igel, P. Mora, B. Riollet, Anisotropic wave propagation through finite-difference grids, Geophysics 60 (1995) 1203–1216.
[8] E. Tessmer, 3-d seismic modelling of general material anisotropy in the presence of the free surface by a Chebyshev spectral method, Geophys. J. Int. 121 (1995) 557–575.
[9] E. Chaljub, et al., 3-D numerical simulations of earthquake ground motion in sedimentary basins: testing accuracy through stringent models, Geophys. J. Int. 201 (2015) 90–111.
[10] J. Kristek, P. Moczo, E. Chaljub, M. Kristekova, An orthorhombic representation of a heterogeneous medium for the finite-difference modelling of seismic wave propagation, Geophys. J. Int. 208 (2017) 1250–1264.
[11] E. Tessmer, D. Kosloff, 3-d elastic modelling with surface topography by a Chebyshev spectral method, Geophysics 59 (1994) 464–473.
[12] H. Igel, Wave propagation in three-dimensional spherical sections by the Chebyshev spectral method, Geophys. J. Int. 136 (1999) 559–566.
[13] A.T. Patera, A spectral-element method for fluid dynamics: laminar flow in a channel expansion, J. Comput. Phys. 144 (1984) 45–58.
[14] E. Priolo, J. Carcione, G. Seriani, Numerical simulation of interface waves by high-order spectral modeling techniques, J. Comput. Phys. 144 (1984) 45–58.
[15] D. Komatitsch, J. Vilotte, The spectral-element method: an efficient tool to simulate the seismic response of 2D and 3D geological structures, Bull. Seismol. Soc. Am. 88 (1998) 368–392.
[16] G. Seriani, 3-D large-scale wave propagation modeling by a spectral-element method on a Cray T3E multiprocessor, Comput. Methods Appl. Mech. Eng. 164 (1998) 235–247.
[17] D. Komatitsch, J. Tromp, Introduction to the spectral-element method for 3-d seismic wave propagation, Geophys. J. Int. 139 (1999) 806–822.
[18] D. Komatitsch, J. Tromp, Spectral-element simulations of global seismic wave propagation—I. Validation, Geophys. J. Int. 149 (2002) 390–412.
[19] G. Scovazzi, B. Carnes, Weak boundary conditions for wave propagation problems in confined domains: formulation and implementation using a variational multiscale method, Comput. Methods Appl. Mech. Eng. 221–222 (2012) 117–131.
[20] T. Song, G. Scovazzi, A Nitsche method for wave propagation problems in time domain, Comput. Methods Appl. Mech. Eng. 293 (2015) 481–521.
[21] G. Scovazzi, T. Song, X. Zeng, A velocity/stress mixed stabilized nodal finite element for elastodynamics: analysis and computations with strongly and weakly enforced boundary conditions, Comput. Methods Appl. Mech. Eng. 325 (2017) 532–576.
[22] M. Käser, V. Hermann, J. de la Puente, Quantitative accuracy analysis of the discontinuous Galerkin method for seismic wave propagation, Geophys. J. Int. 173 (2008) 990–999.
[23] P. Moczo, J. Kristek, M. Galis, P. Pazak, On accuracy of the finite-difference and finite-element schemes with respect to P-wave to S-wave speed ratio, Geophys. J. Int. 182 (2010) 493–510.

[24] M. Kristeková, J. Kristek, P. Moczo, S. Day, Misfit criteria for quantitative comparison of seismograms, Bull. Seismol. Soc. Am. 96 (2006) 1836–1850.
[25] M. Kristeková, J. Kristek, P. Moczo, Time-frequency misfit and goodness-of-fit criteria for quantitative comparison of time signals, Geophys. J. Int. 178 (2009) 813–825.
[26] N. Chevaugeon, K. Hillewaert, X. Gallez, P. Ploumhans, J. Remacle, Optimal numerical parameterization of discontinuous Galerkin method applied to wave propagation problems, J. Comput. Phys. 223 (2007) 188–207.
[27] M. Käser, M. Dumbser, An arbitrary high-order discontinuous Galerkin method for elastic waves on unstructured meshes – I. The two-dimensional isotropic case with external source terms, Geophys. J. Int. 166 (2006) 855–877.
[28] M. Dumbser, M. Käser, An arbitrary high-order discontinuous Galerkin method for elastic waves on unstructured meshes – II. The three-dimensional isotropic case, Geophys. J. Int. 167 (2006) 319–336.
[29] M. Käser, M. Dumbser, J. de la Puerte, H. Igel, An arbitrary high-order Discontinuous Galerkin method for elastic waves on unstructured meshes – III. Viscoelastic attenuation, Geophys. J. Int. 168 (2007) 224–242.
[30] J. de la Puerte, M. Käser, M. Dumbser, H. Igel, An arbitrary high-order discontinuous Galerkin method for elastic waves on unstructured meshes – IV. Anisotropy, Geophys. J. Int. 169 (2007) 1210–1228.
[31] M. Dumbser, M. Käser, E.F. Toro, An arbitrary high-order discontinuous Galerkin method for elastic waves on unstructured meshes – V. Local time stepping and p-adaptivity, Geophys. J. Int. 171 (2007) 695–717.
[32] M. Grote, A. Schneebeli, D. Schötzau, Discontinuous Galerkin finite element method for the wave equation, SIAM J. Numer. Anal. 44 (2006) 2408–2431.
[33] P. Antonietti, I. Mazzieri, A. Quarteroni, F. Rapetti, Non-conforming high order approximations of the elastodynamics equation, Comput. Methods Appl. Mech. Eng. 209–212 (2012) 212–238.
[34] P. Antonietti, C. Marcati, I. Mazzieri, A. Quarteroni, High order discontinuous Galerkin methods on simplicial elements for the elastodynamics equation, Numer. Algorithms 71 (2016) 181–206.
[35] A. Taube, M. Dumbser, C. Munz, R. Schneider, A high order discontinuous Galerkin method with local time stepping for the Maxwell equations, Int. J. Numer. Model. 22 (2009) 77–103.
[36] M. Grote, T. Mitkova, High-order explicit local time-stepping methods for damped wave equations, J. Comput. Appl. Math. 239 (2013) 270–289.
[37] M. Grote, T. Mitkova, Explicit local time-stepping methods for Maxwell's equations, J. Comput. Appl. Math. 234 (2010) 3283–3302.
[38] J. Diaz, M.J. Grote, Energy conserving explicit local time-stepping for second-order wave equations, SIAM J. Sci. Comput. 31 (2009) 1985–2014.
[39] J. Diaz, M.J. Grote, Multi-level explicit local time-stepping methods for second-order wave equations, Comput. Methods Appl. Mech. Eng. 291 (2015) 240–265.
[40] M. Dumbser, V. Casulli, A staggered semi-implicit spectral discontinuous Galerkin scheme for the shallow water equations, Appl. Math. Comput. 219 (15) (2013) 8057–8077.
[41] M. Tavelli, M. Dumbser, A high order semi-implicit discontinuous Galerkin method for the two dimensional shallow water equations on staggered unstructured meshes, Appl. Math. Comput. 234 (2014) 623–644.
[42] M. Tavelli, M. Dumbser, A staggered arbitrary high order semi-implicit discontinuous Galerkin method for the two dimensional incompressible Navier–Stokes equations, Comput. Fluids 119 (2015) 235–249.
[43] M. Tavelli, M. Dumbser, A staggered, space–time discontinuous Galerkin method for the three-dimensional incompressible Navier–Stokes equations on unstructured tetrahedral meshes, J. Comput. Phys. 319 (2016) 294–323.
[44] F. Fambri, M. Dumbser, Spectral semi-implicit and space–time discontinuous Galerkin methods for the incompressible Navier–Stokes equations on staggered Cartesian grids, Appl. Numer. Math. 110 (2016) 41–74.
[45] M. Tavelli, M. Dumbser, A pressure-based semi-implicit space–time discontinuous Galerkin method on staggered unstructured meshes for the solution of the compressible Navier–Stokes equations at all Mach numbers, J. Comput. Phys. 341 (2017) 341–376.
[46] F. Fambri, M. Dumbser, Semi-implicit discontinuous Galerkin methods for the incompressible Navier–Stokes equations on adaptive staggered Cartesian grids, Comput. Methods Appl. Mech. Eng. 324 (2017) 170–203.
[47] F. Harlow, J. Welch, Numerical calculation of time-dependent viscous incompressible flow of fluid with a free surface, Phys. Fluids 8 (1965) 2182–2189.
[48] A. Chorin, A numerical method for solving incompressible viscous flow problems, J. Comput. Phys. 2 (1967) 12–26.
[49] A. Chorin, Numerical solution of the Navier–Stokes equations, Math. Comput. 23 (1968) 341–354.
[50] J.B. Bell, P. Coletta, H.M. Glaz, A second-order projection method for the incompressible Navier–Stokes equations, J. Comput. Phys. 85 (1989) 257–283.
[51] V. Casulli, R.T. Cheng, Semi-implicit finite difference methods for three-dimensional shallow water flow, Int. J. Numer. Methods Fluids 15 (1992) 629–648.
[52] V. Patankar, Numerical Heat Transfer and Fluid Flow, Hemisphere Publishing Corporation, 1980.
[53] J. van Kan, A second-order accurate pressure correction method for viscous incompressible flow, SIAM J. Sci. Stat. Comput. 7 (1986) 870–891.
[54] D. Balsara, D. Spicer, A staggered mesh algorithm using high order Godunov fluxes to ensure solenoidal magnetic fields in magnetohydrodynamic simulations, J. Comput. Phys. 149 (1999) 270–292.
[55] D.S. Balsara, Divergence-free adaptive mesh refinement for magnetohydrodynamics, J. Comput. Phys. 174 (2001) 614–648.
[56] V. Casulli, A semi-implicit numerical method for the free-surface Navier–Stokes equations, Int. J. Numer. Methods Fluids 74 (2014) 605–622.
[57] M. Dumbser, V. Casulli, A conservative, weakly nonlinear semi-implicit finite volume scheme for the compressible Navier–Stokes equations with general equation of state, Appl. Math. Comput. 272 (2016) 479–497.
[58] J. Kristek, P. Moczo, M. Galis, Stable discontinuous staggered grid in the finite-difference modelling of seismic motion, Geophys. J. Int. 183 (2010) 1401–1407.
[59] F. Rubio, M. Hanzich, A. Farrés, J. de la Puente, J.M. Cela, Finite-difference staggered grids in GPUs for anisotropic elastic wave propagation simulation, Comput. Geosci. 70 (2014) 181–189.
[60] J. de la Puente, M. Ferrar, M. Hanzich, J. Castillo, J. Cela, Mimetic seismic wave modeling including topography on deformed staggered grids, Geophysics 79 (2014) T125–T141.
[61] E. Chung, C. Lee, A staggered discontinuous Galerkin method for the convection–diffusion equation, J. Numer. Math. 20 (2012) 1–31.
[62] E. Chung, P. Ciarlet, T. Yu, Convergence and superconvergence of staggered discontinuous Galerkin methods for the three-dimensional Maxwell's equations on Cartesian grids, J. Comput. Phys. 235 (2013) 14–31.
[63] E. Chung, B. Engquist, Optimal discontinuous Galerkin methods for wave propagation, SIAM J. Numer. Anal. 44 (2006) 2131–2158.
[64] E. Chung, B. Engquist, Optimal discontinuous Galerkin methods for the acoustic wave equation in higher dimensions, SIAM J. Numer. Anal. 47 (2009) 3820–3848.
[65] E. Chung, T. Yu, Staggered-grid spectral element methods for elastic wave simulations, J. Comput. Appl. Math. 285 (2015) 132–150.
[66] Y.J. Liu, C.W. Shu, E. Tadmor, M. Zhang, Central discontinuous Galerkin methods on overlapping cells with a non-oscillatory hierarchical reconstruction, SIAM J. Numer. Anal. 45 (2007) 2442–2467.
[67] Y.J. Liu, C.W. Shu, E. Tadmor, M. Zhang, L2-stability analysis of the central discontinuous Galerkin method and a comparison between the central and regular discontinuous Galerkin methods, Math. Model. Numer. Anal. 42 (2008) 593–607.
[68] J.J.W. van der Vegt, H. van der Ven, Space–time discontinuous Galerkin finite element method with dynamic grid motion for inviscid compressible flows I. General formulation, J. Comput. Phys. 182 (2002) 546–585.

[69] H. van der Ven, J.J.W. van der Vegt, Space–time discontinuous Galerkin finite element method with dynamic grid motion for inviscid compressible flows II. Efficient flux quadrature, Comput. Methods Appl. Mech. Eng. 191 (2002) 4747–4780.

[70] C.M. Klaij, J.J.W. van der Vegt, H. van der Ven, Space–time discontinuous Galerkin method for the compressible Navier–Stokes equations, J. Comput. Phys. 217 (2006) 589–611.

[71] S. Rhebergen, B. Cockburn, A space–time hybridizable discontinuous Galerkin method for incompressible flows on deforming domains, J. Comput. Phys. 231 (2012) 4185–4204.

[72] S. Rhebergen, B. Cockburn, J.J. van der Vegt, A space–time discontinuous Galerkin method for the incompressible Navier–Stokes equations, J. Comput. Phys. 233 (2013) 339–358.

[73] M. Balazsova, M. Feistauer, On the stability of the ALE space–time discontinuous Galerkin method for nonlinear convection–diffusion problems in time-dependent domains, Appl. Math. 60 (2015) 501–526.

[74] M. Balazsova, M. Feistauer, M. Hadrava, A. Kosik, On the stability of the space–time discontinuous Galerkin method for the numerical solution of nonstationary nonlinear convection–diffusion problems, J. Numer. Math. 23 (2015) 211–233.

[75] P. Antonietti, I. Mazzieri, A. Quarteroni, F. Rapetti, High order space–time discretization for elastic wave propagation problems, in: M. Azaiez, H.E. Fekihand, J. Hestaven (Eds.), Proceedings of ICOSAHOM 2012, in: Lect. Notes Comput. Sci. Eng., vol. 95, Springer Verlag, 2014, pp. 87–97.

[76] P. Antonietti, N.D. Santo, I. Mazzieri, A. Quarteroni, A high-order discontinuous Galerkin approximation to ordinary differential equations with applications to elastodynamics, IMA J. Numer. Anal., https://doi.org/10.1093/imanum/drx062.

[77] A. Bedford, D. Drumheller, Elastic Wave Propagation, Wiley, Chichester, UK, 1994.

[78] M. Tavelli, M. Dumbser, A staggered arbitrary high order semi-implicit discontinuous Galerkin method for the two dimensional incompressible Navier–Stokes equations, Appl. Math. Comput. 248 (2014) 70–92.

[79] A. Bermudez, A. Dervieux, J. Desideri, M. Vazquez, Upwind schemes for the two-dimensional shallow water equations with variable depth using unstructured meshes, Comput. Methods Appl. Mech. Eng. 155 (1998) 49–72.

[80] A. Bermúdez, J. Ferrín, L. Saavedra, M. Vázquez-Cendón, A projection hybrid finite volume/element method for low-Mach number flows, J. Comput. Phys. 271 (2014) 360–378.

[81] S. Busto, J. Ferrín, E. Toro, M. Vázquez-Cendón, A projection hybrid high order finite volume/finite element method for incompressible turbulent flows, J. Comput. Phys. 353 (2018) 169–192.

[82] E.F. Toro, A. Hidalgo, M. Dumbser, FORCE schemes on unstructured meshes I: conservative hyperbolic systems, J. Comput. Phys. 228 (2009) 3368–3389.

[83] M. Dumbser, A. Hidalgo, M. Castro, C. Parés, E.F. Toro, FORCE schemes on unstructured meshes II: non-conservative hyperbolic systems, Comput. Methods Appl. Mech. Eng. 199 (2010) 625–647.

[84] Y. Saad, M. Schultz, GMRES: a generalized minimal residual algorithm for solving nonsymmetric linear systems, SIAM J. Sci. Stat. Comput. 7 (1986) 856–869.

[85] M. Dumbser, M. Facchini, A local space–time discontinuous Galerkin method for Boussinesq-type equations, Appl. Math. Comput. 272 (2016) 336–346.

[86] A. Breuer, A. Heinecke, M. Bader, C. Pelties, Accelerating SeisSol by generating vectorized code for sparse matrix operators, Adv. Parallel Comput. 25 (2014) 347–356.

[87] A. Breuer, A. Heinecke, S. Rettenberger, M. Bader, A. Gabriel, C. Pelties, Sustained petascale performance of seismic simulations with Seissol on SuperMUC, in: Lecture Notes in Computer Science (LNCS), vol. 8488, 2014, pp. 1–18.

[88] M. Dumbser, D.S. Balsara, E.F. Toro, C.D. Munz, A unified framework for the construction of one-step finite-volume and discontinuous Galerkin schemes, J. Comput. Phys. 227 (2008) 8209–8253.

[89] G. Karypis, V. Kumar, Multilevel k-way partitioning scheme for irregular graphs, J. Parallel Distrib. Comput. 48 (1998) 96–129.

[90] J. de la Puente, J. Ampuero, M. Käser, Dynamic rupture modeling on unstructured meshes using a discontinuous Galerkin method, J. Geophys. Res., Solid Earth 114 (2012) B10302.

[91] C. Pelties, J. de la Puente, J. Ampuero, G. Brietzke, M. Käser, Three-dimensional dynamic rupture simulation with a high-order discontinuous Galerkin method on unstructured tetrahedral meshes, J. Geophys. Res., Solid Earth 117 (2012) B02309.

[92] O. Zanotti, F. Fambri, M. Dumbser, A. Hidalgo, Space–time adaptive ADER discontinuous Galerkin finite element schemes with a posteriori sub-cell finite volume limiting, Comput. Fluids 118 (2015) 204–224.

[93] S.K. Godunov, E.I. Romenski, Nonstationary equations of the nonlinear theory of elasticity in Euler coordinates, J. Appl. Mech. Tech. Phys. 13 (1972) 868–885.

[94] I. Peshkov, E. Romenski, A hyperbolic model for viscous Newtonian flows, Contin. Mech. Thermodyn. 28 (2016) 85–104.

[95] M. Dumbser, I. Peshkov, E. Romenski, O. Zanotti, High order ADER schemes for a unified first order hyperbolic formulation of continuum mechanics: viscous heat-conducting fluids and elastic solids, J. Comput. Phys. 314 (2016) 824–862.

[96] M. Dumbser, I. Peshkov, E. Romenski, O. Zanotti, High order ADER schemes for a unified first order hyperbolic formulation of Newtonian continuum mechanics coupled with electro-dynamics, J. Comput. Phys. 348 (2017) 298–342.

[97] D. Balsara, R. Käppeli, Von Neumann stability analysis of globally divergence-free RKDG schemes for the induction equation using multidimensional Riemann solvers, J. Comput. Phys. 336 (2017) 104–127.

[98] M. Dumbser, D. Balsara, M. Tavelli, F. Fambri, A divergence-free semi-implicit finite volume scheme for ideal, viscous and resistive magnetohydrodynamics, Int. J. Numer. Methods Fluids (2018), submitted for publication, https://arxiv.org/abs/1801.06592.

[99] D. Balsara, A. Taflove, S. Garain, G. Montecinos, Computational electrodynamics in material media with constraint-preservation, multidimensional Riemann solvers and sub-cell resolution – Part I, second-order FVTD schemes, J. Comput. Phys. 349 (2017) 604–635.

[100] D. Balsara, S. Garain, A. Taflove, G. Montecinos, Computational electrodynamics in material media with constraint-preservation, multidimensional Riemann solvers and sub-cell resolution – Part II, higher order FVTD schemes, J. Comput. Phys. 354 (2018) 613–645.